Green Chemistry

PAPER

View Article Online
View Journal | View Issue

Cite this: *Green Chem.*, 2024, **26**, 7212

Carbon-negative hydrogen: aqueous phase reforming (APR) of glycerol over NiPt bimetallic catalyst coupled with CO_2 sequestration†

Leoncio Santiago-Martínez, [a,b] Mengting Li,[a] Paola Munoz-Briones, [a] Javiera Vergara-Zambrano, [a] Styliani Avraamidou,[a] James A. Dumesic [a] and George W. Huber [a]*

Herein we report the production of high-pressure (19.3 bar), carbon-negative hydrogen (H_2) from glycerol with a purity of 98.2 mol% H_2, 1.8 mol% light hydrocarbons (mainly methane), and 400 ppm of CO. Aqueous phase reforming (APR) of 10 wt% glycerol solution was studied with a series of NiPt alumina bimetallic catalysts supported on alumina. The Ni_8Pt_1-450 catalyst had the highest hydrogen selectivity (95.6%) and the lowest alkanes selectivity (3.7%) of the tested catalysts. The hydrogen selectivity decreased in the order of Ni_8Pt_1-450 > Ni_8Pt_1-260 > Ni_1Pt_1-260 > Pt-260. The CO_2 was sequestered with CaO adsorbent which formed $CaCO_3$. We measured the adsorption capacity of the CaO adsorbent at different temperatures. Life cycle analysis showed that the APR of glycerol coupled with CO_2 capture has net negative CO_2 equivalent greenhouse gas emissions. The CO_2 emissions are −9.9 kg CO_2 eq./kg H_2 and −50.1 kg CO_2 eq./kg H_2 when grid electricity and renewable electricity are used, respectively, and the CO_2 is allocated respectively to the mass of products produced. The cost of this H_2 (denoted as "green-emerald") was estimated to be 2.4 USD per kg H_2 when grid electricity is used and 2.7 USD per kg H_2 when using renewable electricity. The cost of glycerol has the highest contribution of 1.71 USD per kg H_2. Participation in the carbon credit markets can further decrease the price of the produced H_2.

Received 17th April 2024,
Accepted 15th May 2024

DOI: 10.1039/d4gc01896f

rsc.li/greenchem

1. Introduction

Hydrogen (H_2) is an important chemical in refining processes, ammonia production, energy storage, and as an alternative and cleaner fuel.[1] Hydrogen is mainly produced from steam reforming of natural gas (grey H_2), and coal gasification (black H_2). These processes emit 8.5 to 12.9 kg CO_2/kg H_2 and 18 to 26 kg CO_2/kg H_2, respectively.[2–7] To reduce the emissions associated with H_2 production, an array of new technologies are under development, all of which produce H_2 with a different emission level and energy source. Table 1 shows the H_2 types and colors used to identify H_2 types according to the Global Energy Infrastructure (GEI).[8] Pink, turquoise, and green H_2 have the lowest emissions ranging from 0 to 5.1 kg CO_2/kg H_2. Blue H_2 is considered a low-carbon emissions hydrogen with as low as 0.7 kg CO_2/kg H_2, but could emit even 13 kg CO_2/kg H_2 due to fugitive methane emissions.[5]

The importance of sustainably produced H_2 has been highlighted recently by the U.S. Department of Energy through the establishment of the 2020 H_2 Program Plan[15] to develop pathways to produce carbon-neutral H_2 (0 kg CO_2/kg H_2) and carbon-negative H_2 (<0 kg CO_2/kg H_2) at a low cost. The price target is 2.00 USD per kg of H_2 production for transportation applications and 1.00 USD per kg for industrial and stationary power generation applications. The low-carbon H_2 sources include H_2 production from renewable sources like biomass or waste conversion, from water splitting using renewable electricity (green H_2), and from natural gas steam reforming with carbon capture utilization and storage (CCUS) (blue H_2).

Biomass captures CO_2 from the atmosphere during the process of photosynthesis. Using biomass to produce H_2 offers the advantage of producing H_2 from a low-carbon source. Combining H_2 production from biomass with carbon capture and storage during H_2 production has the potential to produce carbon-negative H_2.[16] High-pressure H_2 can be produced from biomass-derived sugar alcohols (ethylene glycol, glycerol, or sorbitol) through aqueous phase reforming (APR).[17–22] Biomass-derived H_2 can be classified as carbon-negative H_2 when the CO_2 is captured or sequestrated, as shown in Fig. 1. High-pressure CO_2 and H_2 are produced from APR. This CO_2 can be chemically trapped in the carbonation process with the

[a]*Department of Chemical and Biological Engineering, University of Wisconsin, Madison, WI 53706, USA. E-mail: gwhuber@wisc.edu*
[b]*DOE Center for Advanced Bioenergy and Bioproducts Innovation, University of Illinois at Urbana-Champaign, Urbana, IL, USA*
† Electronic supplementary information (ESI) available. See DOI: https://doi.org/10.1039/d4gc01896f

Table 1 Hydrogen types and color classification. Adapted from GEI[8]

Hydrogen color/type	Source	Hydrogen production process	CO_2 emissions (kg CO_2/kg H_2)	Ref.
Green	Water	Electrolysis with renewable electricity (wind, solar, hydro)	0–5.1	2–6
Purple/pink/red		Electrolysis using nuclear energy	0–0.6	2,4 and 6
Yellow		Electrolysis using mixed-origin grid energy	14.5–28.6	4 and 5
Blue	Natural gas coal	Natural gas steam reforming or coal gasification with CCUS	0.7–13	2–6
Turquoise	Natural gas	Pyrolysis of natural gas	1.9–4.8	2
Grey		Natural gas steam reforming	8.5–12.9	2–6
Brown	Lignite	Lignite gasification	20–25.3	6 and 7
Black	Coal	Coal gasification	18.0–26	2–7
Aqua	Oil sands or conventional oil fields	Oxygen injection into heavy oil reservoirs or oil sands deep underground	0	6 and 9
Gold	Underground deposits	Refers to hydrogen produced by fermenting microbes in depleted oil wells or naturally occurring H_2	Not available	10–12
White		Naturally occurring H_2	Not available	13
Orange		Induced by injecting water in reactive formations	Not available	13
Not classified	Biomass	Biomass (wood chips, and corn stover) gasification	0.41–2.68	3 and 4
		Wood chips gasification with CCUS	−21–(−16)	4
		Ethanol reforming	9.19–14	3
		APR of glycerol	3.88–4.11	14

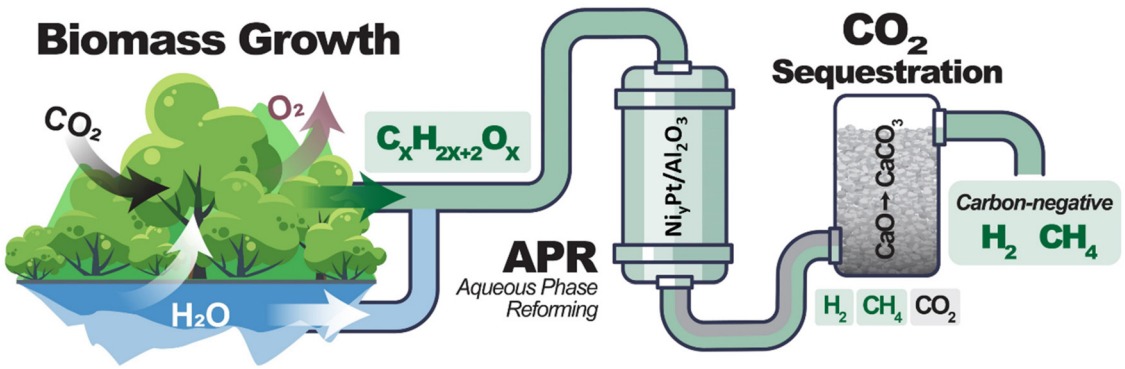

Fig. 1 Schematic representation of a process to produce carbon-negative H_2 from biomass-derived compounds through aqueous phase reforming (APR) technology and CO_2 sequestration.

possibility of storing the carbon in geological Ca formations in the form of $CaCO_3$. Thus, there is no direct CO_2 emitted to the atmosphere during the process. Carbon capture usage and storage (CCUS) has been applied to the field of biomass conversion,[23–27] primarily in the biomass gasification process with *in situ* CO_2 adsorption. For example, Xu *et al.*[26] reported the use of Fe/CaO catalyst for wood sawdust gasification to H_2-rich syngas production, in which the presence of iron improves the CO_2 adsorption capacity of CaO. Doranehgard *et al.*[27] reported the use of CaO to improve tar cracking and reduce CO_2 emissions in rice husk gasification. Han *et al.*[24] found that pressurized sawdust gasification instead of atmospheric gasification in CaO, produces syngas with a higher H_2 and lower CO_2 content by promoting the gasification reactions and the CaO carbonation. However, gasification processes are typically carried out at low pressure, and they therefore require downstream compression of the H_2.

Whole biomass,[28,29] cellulose,[30–33] and xylose[34–36] have all been used as feedstocks for APR. Valenzuela *et al.*[28] reported the APR of Southern pine sawdust, using sulfuric acid (2 M) and Pt/Al_2O_3 catalyst at 225 °C in a batch reactor. Wen *et al.*[32] reported that the use of Pt/C can convert the cellulose efficiently into H_2 in a one-pot APR at 260 °C, with 40% H_2 selectivity. Later they used[31] a Ce-modified RANEY® Ni catalysts at the same (260 °C) temperature and reported an increased H_2 selectivity and decreased methane selectivity when large quantities of Ce were added at a Ce : Ni ratio of 0.054. All these studies were carried out in batch reactors with a biomass slurry feed. Industrially it is not practical to perform APR in batch reactors.

Hydrogen selectivity in the APR depends on the reaction conditions and the catalysts used. Several studies[18,20,37–44,45–49] reported reaction temperatures from 210 °C to 250 °C, with system pressures between 2 to 7 bar above the bubble point of water to maintain the non-volatile feedstock in the liquid phase. In some cases,[37,50–54] the system pressure was varied from 10 to 21 bar above the bubble point of water. Davda *et al.*[19] and Shabaker *et al.*[17] reported that an increase in the total system pressure inhibits H_2 production. Huber *et al.*[18] studied the use of bimetallic PtNi over alumina, with a Pt : Ni

molar ratio of 1 : 1, 1 : 5, and 1 : 8 for the APR of ethylene glycol at 210 °C. Their findings indicate that a Pt : Ni ratio of 1 : 5 has a higher H_2 selectivity (91.2%), and no alkane production compared to the pure Pt-based catalyst. El Doukkali *et al.*[37] reported the use of a bimetallic PtNi catalyst over alumina, prepared by a sol–gel method containing 8 wt% Ni. This PtNi catalyst was more active for the APR process of glycerol than other bimetallic catalysts (PtFe, PtCo) or monometallic Ni or Pt over alumina. However, the H_2 selectivity (40%) was lower than with the monometallic Pt catalyst. Other authors[37,38,55,56] reported similar conclusions for the NiPt bimetallic catalysts for different Ni loadings, ranging from 0.75 wt% to 12 wt%.

Several authors[57–65] have reported the use of CaO as a sorbent for carbon mineralization. Hlaing *et al.*[66] reported that CaO derived from aragonite reached an adsorption capacity of 0.125 mol CO_2/mol CaO at 300 °C and 0.869 mol CO_2/mol CaO at 700 °C. The carbonation temperature was the most important factor affecting the CaO adsorption capacity. The CO_2 capture can be improved by the presence of steam[61] in the flue gases during the carbonation at 650 °C or a pre-hydration step[65] of the CaO for carbonation at room temperature. Using regenerable solvents in a water solution, such as monoethanolamine or sodium glycinate, can improve carbon mineralization by a single step of CO_2 capture and carbon mineralization at low temperatures.[64,67]

G. Gadikota and A. A. Park[68] reported that calcium and magnesium-bearing minerals such as wollastonite, olivine, or serpentine could be used for CO_2 mineralization, since they contain non-carbonated Ca or Mg. There are two approaches for CO_2 sequestration using minerals: *in situ* or *ex situ* carbon mineralization. The *in situ* carbon mineralization involves the injection of high-pressure CO_2 in geological formations containing Ca and/or Mg minerals. For this approach, the CO_2 needs to be separated from the hydrogen stream produced in the APR of biobased feedstocks and injected underground. Pressure swing adsorption (PSA)[69] can be used to separate the CO_2 and produce a high-purity H_2 (>98%) stream. PSA has the advantage of low temperature (≈25 °C) operation, pressures between 20 and 40 bar, hydrogen recovery higher than 90%, and the adsorbent can last for several years. In *ex situ* mineralization, the minerals need to be mined, grounded, and reacted in adsorbers/reactors. The carbonated minerals can be deposited in geological formations or can be used in applications such as filler materials, coatings, construction materials, liming agents to neutralize soil acidity, or remediation of contaminated lands.[68]

In this study we decided to first use glycerol as a feedstock because of it ease to analyze in the process and to demonstrate integration with carbon capture. APR with carbon capture can have more of an impact when integrated with more abundant feedstocks such as biomass-derived sugar alcohols, xylose, cellulose, or whole biomass. According to the U.S. Department of Energy,[15] over a billion tons of dry feedstock, including biomass and waste-stream resources, can be used for sustainable hydrogen production. Thus, future work should focus on how to integrate green-emerald hydrogen production with more abundant biomass feedstocks. The study focuses only on glycerol produced in a restricted area of the U.S. (Wisconsin area) to facilitate the techno-economic, and life cycle analysis. Improved catalysts, with increased stability, selectivity, and activity, are needed if APR is to be implemented commercially.

In this work, we report for the first time, the production of carbon-negative H_2 from glycerol using APR coupled with CO_2 sequestration by CaO carbonation, producing a high-pressure carbon-negative H_2 stream with 98.2% of purity. We will denote this type of H_2 as "green-emerald" to differentiate it from the other common types of H_2 reported in Table 1. We perform an LCA and economic analysis using our experimental data to estimate the economics and environmental impacts of producing H_2 by aqueous phase reforming coupled with CaO adsorption to separate H_2 from CO_2.

2. Methods

2.1. Catalyst preparation and characterization

Monometallic Pt/γ-Al_2O_3 and bimetallic Ni_xPt_1/γ-Al_2O_3 catalysts were prepared by incipient wetness impregnation, using Catapal B γ-Al_2O_3 of Sasol as the support. Catapal B was dried in a vacuum oven (VWR Symphony) at 60 °C for two hours before the impregnation. Pt/γ-Al_2O_3 with 3 wt% Pt (Pt-260) was prepared using 1 mL of tetraamine platinum(II) nitrate (Sigma-Aldrich) solution per gram of dried support. The catalyst was dried for 2–3 hours and calcined at 260 °C for two hours in a tube furnace using a heating rate of 1 °C min^{-1} and 100 mL min^{-1} of air. The calcined catalyst was milled in a mortar until fine powder and used without sieving. To prepare the bimetallic catalysts Ni_1Pt_1/γ-Al_2O_3 (Ni_1Pt_1-260) and Ni_8Pt_1/γ-Al_2O_3, a similar procedure was followed, using 1 mL of nickel nitrate hexahydrate solution to get a Ni to Pt atomic ratio of 1 : 1 and 8 : 1. The impregnated samples were dried and calcined similarly as previously described.

The prepared catalyst was reduced by flowing 100 mL min^{-1} of hydrogen for two hours at 260 °C, with a heating rate of 1 °C min^{-1}. After the reduction, the samples were passivated for 30 min using a 1 vol% O_2/Argon before the characterization with CO chemisorption. For the Ni_8Pt_1/γ-Al_2O_3 catalyst, two reduction temperatures were applied, 260 °C (Ni_8Pt_1-260) and 450 °C (Ni_8Pt_1-450).

2.2. Aqueous phase reforming (APR)

At the beginning of a run, 1.0 g of calcined catalyst was loaded into a 1/4″ SS reactor. The catalyst was fixed at the center of the furnace using silica chips (35 mesh) and 0.1 g of fiberglass plugs to separate the silica beds and the catalyst bed. The reactor was kept at the operation temperature by monitoring the temperature with a K-type thermocouple (Omega) and using an aluminum insert in the furnace. The catalyst was reduced *in situ* at 260 °C for two hours with a heating rate of 1 °C min^{-1}, with 100 mL min^{-1} of 10 vol% H_2/Helium, except for Ni_8Pt_1/γ-Al_2O_3, which was reduced at 450 °C. After the two-hour reduction, the reactor was flushed with nitrogen; mean-

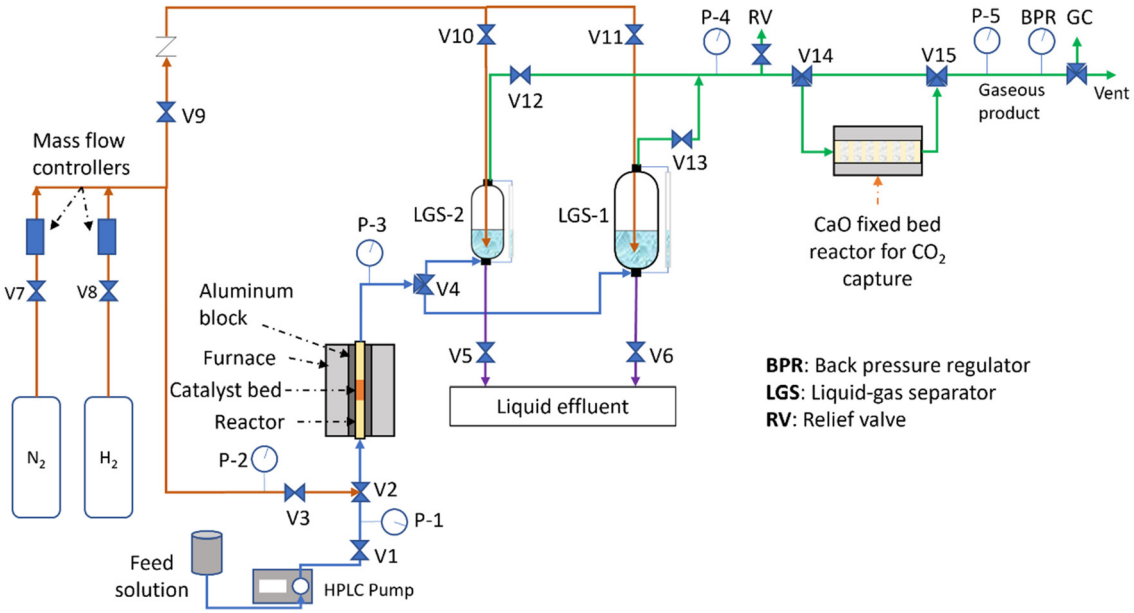

Fig. 2 Scheme of the reactor system used for aqueous phase reforming of glycerol with CO_2 sequestration.

while the temperature decreased to the reaction temperature (209 °C). Then, the APR reaction system (Fig. 2) was pressurized at the operation pressure (typically 0.5 bar above the bubble point of water at the operation temperature) using nitrogen. The pressure was controlled by a backpressure regulator (TESCOM 26-1764-24). Once the pressure was stable, the feed solution consisting of 10 wt% glycerol/water was fed using an HPLC pump at a flow rate of 0.06 mL min^{-1}. The product mixture was separated in the liquid–gas separator vessel, in which nitrogen was used as sweep gas at 45 to 50 mL min^{-1} and bubbled through the liquid phase inside the separator. The gaseous product mixture was then collected and analyzed using a GC (Shimadzu Refinery gas analyzer) equipped with an FID and two TCD detectors. The liquid product collected was analyzed by TOC (Shimadzu TOC-V CPH) to determine the carbon balance. For evaluating the catalysts at different temperatures and pressures, each data point reported in sections 3.1 and 3.2 corresponds to the mean value of three samples taken each two hours between 18 to 26 h of reaction.

Hydrogen selectivity was calculated based on the number of molecules of H_2 produced. The equations used to evaluate the catalyst performance are given in eqn (1)–(4), in which RR is the H_2/CO_2 reforming ratio (7/3 for glycerol).

$$H_2\ \text{selectivity} = \frac{\text{Molecules of } H_2 \text{ produced}}{\text{C atoms in gas phase}}\left(\frac{1}{RR}\right) \times 100 \quad (1)$$

$$\text{Alkanes selectivity} = \frac{\text{C atoms in gaseous alkanes}}{\text{Total C atoms in gas phase product}} \times 100 \quad (2)$$

$$\%\ \text{of glycerol conversion to gas phase} = \frac{\text{C atoms in gas product}}{\text{Total C atoms in the feed}} \times 100 \quad (3)$$

$$\text{TOF} = \frac{\text{mol of } H_2 \text{ produced}}{\text{mol of active sites} \times \text{time}} \quad (4)$$

2.3. CO_2 adsorption

CO_2 adsorption experiments were carried out for the APR of 10 wt% glycerol/water at 209 °C and 19.3 bar over Ni_8Pt_1-450. For CO_2 sequestration, the gas product mixture was passed through a fixed bed reactor packed with commercial CaO from Sigma-Aldrich (4 g, 15 g, and 50 g). The CaO was packed using a 1″ SS tube in which the CaO was packed in beds of 5 g separated with quartz wool, as shown in Fig. 3; the pressure drop along the packed bed was negligible during the adsorption process.

The CO_2 adsorption experiment was carried out first with 50 g of CaO at isothermal conditions at 20, 200, 300, 400, 500, 600, and 700 °C, at the APR reaction system pressure. The adsorption started at room temperature until saturation; then the CO_2 adsorber was heated to a higher isothermal tempera-

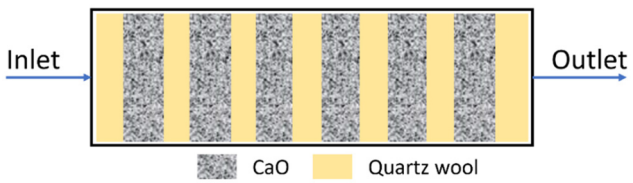

Fig. 3 Schematic representation of the CaO-packed bed reactor for CO_2 sequestration.

ture. On the other hand, for 15 g, and 4 g of CaO, the adsorption was carried out at isothermal conditions at 600 °C. For these experiments, the gas product was sampled at the inlet and the outlet of the CO_2 adsorber for GC analysis.

2.4. CO_2 adsorption modeling

Eqn (1) and (2) were applied to calculate the adsorption constant for CO_2 adsorption over CaO. The CaO bed was considered as a plug-flow reactor. The feed to the bed is a mixture of CO_2 and H_2. The molar flow rate of H_2 is constant, whereas the partial pressure of CO_2 and the molar flow rate of CO_2 decrease through the bed as CaO captures CO_2. We assumed that the capture of CO_2 is first order with respect to the partial pressure of CO_2 as described in eqn (5), where k is the rate constant for CO_2 capture (1/atm-min). The equation to calculate k is described in eqn (6), where F_{H_2} is the molar flow rate of H_2 (mol H_2 per min). F_{N_2} is the molar flow rate of N_2 (mol N_2 per min). P_{CO_2} is the partial pressure of CO_2 (atm). P_{tot} is the total pressure (atm). S_{tot} is the total number of CaO active sites in the reactor (mol sites). Note that S_{tot} is a function of time because the total number of active CaO sites decreases as sites become neutralized by the capture of CO_2. TOF is the turnover frequency of reacting CO_2 with CaO, defined as the rate of CO_2 capture per CaO site per unit time (mol CO_2 per mol site per min).

$$\mathrm{TOF} = kP_{CO_2} \tag{5}$$

$$k(t) = \left\{ \frac{P_{tot}(P^{in}_{CO_2} - P^{out}_{CO_2}(t))}{(P_{tot} - P^{in}_{CO_2})(P_{tot} - P^{out}_{CO_2}(t))} + \ln\left[\frac{(P_{tot} - P^{out}_{CO_2}(t))P^{in}_{CO_2}}{(P_{tot} - P^{in}_{CO_2})P^{out}_{CO_2}(t)}\right] \right\} \frac{(F_{H_2} + F_{N_2})}{P_{tot}S_{tot}(t)} \tag{6}$$

2.5. Life cycle assessment (LCA)

LCA is a tool to quantify the environmental impacts of technologies. LCA was conducted in this study to evaluate the system-wide greenhouse gas (GHG) emissions for hydrogen production. In this study we compared the process in which we coupled APR with CO_2 sequestration using CaO at 600 °C, and the process of APR coupled with Pressure Swing Adsorption (PSA) to obtain a high-purity hydrogen stream. For this analysis, six stages (Fig. 4) were considered: (i) crop cultivation, (ii) seed drying, (iii) transportation, (iv) oil processing & refining, (v) glycerol production, and (vi) H_2 production. Soybeans were used as the crop, as it is one of the most cultivated crops in Wisconsin (USA). Two scenarios for the electricity source are considered, one using the current Wisconsin grid electricity (Scenario A) and the other one using 100% renewable electricity (Scenario B). The methodology followed for carbon sequestration, and impact allocation, along with the list of assumptions and sources are discussed below.

2.5.1 Carbon uptake. The cultivation of soybeans can take up carbon from the atmosphere during photosynthesis and store it as biomass. In addition, cover crops, dead organic matter, and soil can also contribute to carbon uptake.[70]

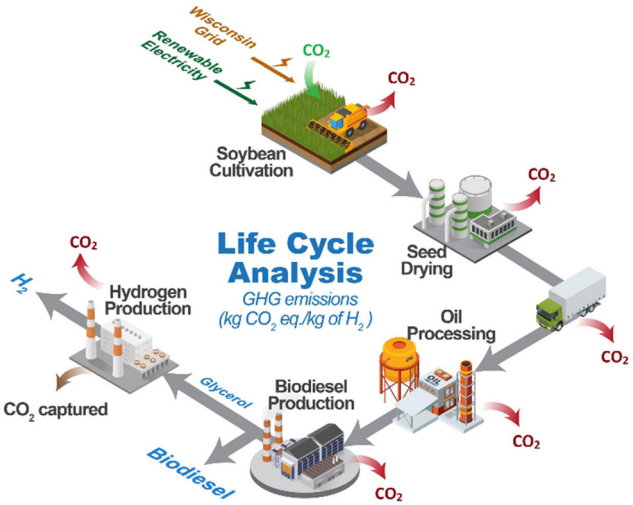

Fig. 4 Hydrogen production pathway and types of GHG emissions. The GHG emissions (red arrows), uptake (green arrow), and capture (brown arrow) of each production stage.

Although soybean cultivation has the potential to sequester carbon, a considerable amount of carbon is released into the atmosphere during the cultivation and harvesting processes, and plant decomposition. Estimating how much carbon is absorbed and not released back into the atmosphere is challenging.[70] For our study, a conservative approach of considering only the carbon content of soybean oil as the amount of carbon absorbed is followed. By focusing on the carbon content of the soybean oil, it is possible to estimate conservatively the CO_2 uptake of soybean cultivation. This method has been adopted by Schmidt,[71] the LCA report conducted by Omni Tech International,[72] and the LCA of bioenergy products in the ecoinvent® 2.01 database developed by Jungbluth *et al.*[73] The biogenetic CO_2 uptake used in our analysis is therefore considered to be −2.823 kg CO_2/kg refined oil.[71]

2.5.2 Impact allocation. This study considers two schemes, mass allocation and carbon allocation, to allocate environmental emissions of the H_2 produced from glycerol, which is the coproduct of biodiesel production. The first approach is based on the mass of glycerol and biodiesel. Physical partitioning is done by dividing the inputs and outputs of a process in a way that reflects the physical relationship of mass, according to the ISO 14044 standard for life cycle assessment (LCA). This approach is widely used as it is straightforward and results in small uncertainty ranges.[72] This mass allocation approach is consistent with the approach adopted in most other life cycle analyses.[72,74]

The second approach considered for allocation is based on the mass of carbon, which represents the actual carbon flow. It is suggested by Leinonen to be a logical choice of allocation method for forestry products.[70] The carbon content of glycerol and biodiesel is determined and used to allocate the total carbon emissions of the production process to each product. Such a carbon allocation method is useful when analyzing the carbon footprint of bio-based products, such as soybean,

where the carbon sequestration and storage of soybean are taken into account based on the quantity of biomass carbon stored in the products. Since not all products considered in the process are used directly to generate energy, the energy allocation was not performed, and carbon allocation is considered to be more appropriate.

2.5.3 Other assumptions and modeling. Other assumptions that were made to estimate the environmental impact of hydrogen production include:

(1) CO_2 generated during H_2 production is captured and sold for carbon credits.

(2) Direct land use refers to the physical occupation or transformation of land for the cultivation of soybean. Indirect land use takes into account the possible substitution of alternative land uses, including agricultural crops or natural ecosystems, as a result of the growing demand for H_2 production from glycerol. These indirect uses were not employed here since the connection between land use and deforestation is not clearly explained and there is a lack of agreement on how to establish this connection.[71] Therefore, land use calculations are not included.

(3) All processes considered (Fig. 4) are assumed to be located in Wisconsin, and it is assumed that the biodiesel and H_2 facilities are located nearby. Therefore, only the transportation of soybean to the oil processing plant is considered. The study assumes that the soybeans are transported to the oil processing plant *via* diesel-fueled trucks.

(4) Seed yield is assumed to be 2889.6 kg (ha year)$^{-1}$ and oil yield is assumed to be 547.4 kg (ha year)$^{-1}$.[75]

(5) GHG emissions of soybean cultivation were based on data from conventional soybean production in the USA.[75]

(6) GHG emissions of biodiesel production were based on data from Dufour and Iribarren.[74]

(7) Two GHG emission allocation methods were considered, one based on mass and one on carbon content, as mentioned above.

(8) The CaO comes from geological formations, and emissions associated with its transportation are considered in the calculation.

(9) For the process of APR coupled with Pressure Swing Adsorption (PSA), we considered that the CO_2 can be injected underground or sold to third parties.

An overview of the mass relationships between various feedstocks and products involved in the process is outlined in Table 2.

This study includes both primary and secondary data. Primary data collected from experiments and process simulations are used to evaluate the GHG emissions of H_2 production using APR from glycerol. The OpenLCA software has been utilized. The data on materials were collected from the database Agribalyse. The ReCiPe 2016 midpoint (H) LCIA method converts the resource consumptions and emissions of the life cycle inventory data into global warming potential (GWP). Secondary data on other producing stages were collected from literature.[71,74,75]

Table 2 The mass of feedstocks and products of each production stage

	Soybean oil production[75]	Biodiesel production[74]	Hydrogen production
Seed (kg)	430.3	—	—
Refined oil (kg)	81.5	81.5	—
Glycerol (kg)	—	6.9	6.9
Biodiesel (kg)	—	67.6	—
Hydrogen (kg)	—	—	1

3. Results and discussion

3.1. Effect of total pressure system on APR of glycerol

A Pt/γ-Al_2O_3 catalyst was used to study glycerol aqueous phase reforming (APR) as a function of temperature and pressure. Table 3 and Fig. 5 show that the H_2 selectivity and production rate decrease as the total system pressure increases. The CO_2 and C2–C3 alkanes selectivity increases with pressure. The catalyst was run for 480 h on stream with low deactivation. The H_2 selectivity (75% at 209 °C) did not change during 523 h after different cycles between temperatures (209 °C–269 °C) and pressures (19.3 bar–57.9 bar); see Fig. S1 in ESI.†

The effect of pressure for APR has been previously described by Davda *et al.*[19] and Shabaker *et al.*[17] with similar observations. Hydrogen inhibits the APR reaction. As shown in Table 3, the mol percent of H_2 and methane decreases when the total pressure increases, while CO_2, ethane, and propane mol percent increase. This behavior indicates that H_2 is consumed in the hydrogenation of C2 and C3 intermediates.

Table 3 APR of glycerol (10 wt%) at 209 °C, and a WHSV of 0.37 h^{-1} over Pt/γ-Al_2O_3. The carbon balance for each experiment was verified to be 100% ± 5.6%

	Gas phase composition (mol%)					Selectivity (%)			H_2 production rate		
P (bar)	H_2	CO_2	CH_4	C_2H_6	C_3H_8	H_2	Alkanes	Glycerol conversion to the gas phase (%)	(μmol μmol$_{Pt}^{-1}$ min^{-1})	(μmol g$_{cat}^{-1}$ min^{-1})	H_2 TOF (min^{-1})
19.3	64.3	32.0	2.8	0.7	0.1	75.1	12.7	25.5	0.65	99.8	1.8
20.0	63.6	32.7	2.7	0.8	0.2	72.8	12.6	22.0	0.54	83.6	1.5
20.7	64.3	32.2	2.6	0.7	0.2	74.9	12.4	22.4	0.57	87.7	1.6
22.1	62.2	34.3	2.5	0.8	0.2	68.5	12.2	17.3	0.40	62.0	1.1
23.4	61.9	34.9	2.1	0.8	0.2	67.4	11.3	11.3	0.26	39.8	0.7

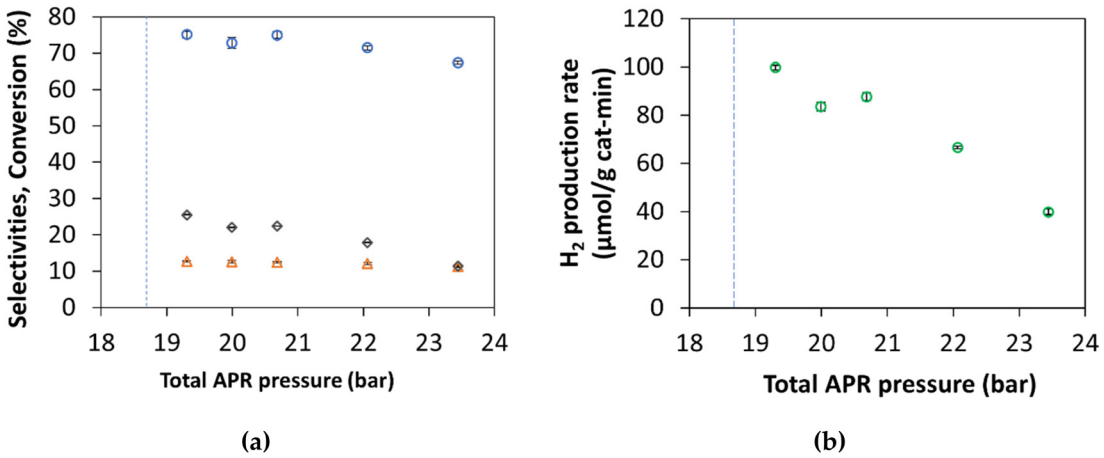

Fig. 5 (a) Hydrogen selectivity (○), alkanes selectivity (Δ), and glycerol conversion (◊) to gas phase; and (b) hydrogen production rate (○), in the aqueous phase reforming of 10 wt% of glycerol at 209 °C, and a WHSV of 0.37 h^{-1} for different total pressures in the system over Pt/γ-Al_2O_3. The blue dashed line indicates the bubble point of water (18.7 bar) at 209 °C. Each data point is the mean value of three samples and the standard deviation is indicated by the error bar.

As shown in Fig. 5 H_2 selectivity and H_2 production rate are highest when the system pressure is close to the bubble point of water. The remainder of the APR studies for this paper were fixed at 0.4–0.6 bar above the bubble point of water.

3.2. Aqueous phase reforming of glycerol with bimetallic NiPt catalysts

Bimetallic NiPt/alumina catalysts were prepared and studied for the APR of glycerol. Table 4 shows the APR of these catalysts at three different temperatures (209, 224, and 241 °C). As illustrated in Fig. 6, the H_2 selectivity increases in the order Ni_8Pt_1 > Ni_1Pt_1 > Pt when the catalysts are reduced *in situ* at 260 °C. There is an additional increase in H_2 selectivity when the Ni_8Pt_1-450 catalyst is reduced at 450 °C. These effects are more visible when APR is carried out at low temperature (209 °C), achieving a H_2 selectivity of 95.7%, and a 3.7% of alkanes selectivity for Ni_8Pt_1-450. The Ni_8Pt_1-450 catalyst was selected for the APR of glycerol coupled with CO_2 sequestration, detailed in the next section.

The gas phase H_2 composition increased from 64.3 mol% at 209 °C with Pt/Al_2O_3 (Pt-260), to 69.1 mol% using the Ni_8Pt_1-450 bimetallic catalyst as shown in Table 4. The H_2 to CO_2 ratio was close to the stoichiometric ratio with only 1.1 mol% of alkanes. The CO concentrations were lower than 10 ppm under all the reaction conditions reported in Table 4.

Previous studies reported[18,37,76] that the use of Ni promotes the water–gas shift reaction, improves the dehydrogenation of adsorbed glycerol, and decreases the strength of H_2 and CO adsorption, preventing the blockage of active sites. Additional studies are needed to understand the effect of Ni addition and the interaction between Ni–Pt, and the support. Tanksale *et al.*[77] found that Ni–Pt forms a metallic alloy over the support, resulting in a synergetic effect and enhanced activity on the APR of glycerol. The improved hydrogen selectivity of the Ni_8Pt_1-450 catalyst compared to Ni_8Pt_1-260 can be explained by the complete reduction of nickel oxide at 450 °C, affecting the crystal form and size.[78] Rahman *et al.*[76] reported that Ni_6Pt, Ni_8Pt, and $Ni_{12}Pt$ supported over Ce-doped alumina support, have similar hydrogen selectivities, with a higher selectivity over Ni_6Pt with 83% and 86% yield on the APR of 1% of glycerol at 240 °C. This behavior is comparable to the selectivity we reported here for Ni_8Pt_1-260 at the same APR temperature (240 °C) but lower than

Table 4 APR of 10 wt% glycerol/water over Pt-supported alumina-based catalysts. The carbon balance for each experiment was verified to be 100% ± 5.6%

					Gas phase composition (mol%)					Selectivity (%)			H_2 production rate		
Catalyst	CO chemisorption (µmol g^{-1})	WHSV (h^{-1})	T (°C)	P (bar)	H_2	CO_2	CH_4	C_2H_6	C_3H_8	H_2	Alkanes	Glycerol conversion to gas phase (%)	(µmol H_2 g_{cat}^{-1} min^{-1})	(µmol H_2 $µmol_{Pt}^{-1}$ min^{-1})	TOF (min^{-1})
Pt-260	57.4	0.37	209	19.3	64.3	32.0	2.8	0.7	0.1	75.1	12.7	25.5	99.7	0.6	1.7
			224	26.9	63.4	32.3	3.3	0.9	0.2	71.8	14.5	42.0	157.2	1.0	2.7
			240	34.5	62.4	32.3	4.0	1.1	0.2	68.5	17.4	74.5	267.3	1.7	5.4
Ni_1Pt_1-260	39.1	0.37	209	19.3	66.2	31.3	2.3	0.2	0.0	83.3	8.1	46.9	203.3	1.3	5.2
			224	25.5	66.5	30.1	3.1	0.3	0.0	84.0	11.3	65.7	287.1	1.9	7.3
			241	34.5	65.2	29.8	4.4	0.5	0.1	78.8	16.0	84.1	345.3	2.2	8.8
Ni_8Pt_1-260	38.7	0.36	209	19.3	68.1	30.4	1.4	0.1	0.0	91.3	5.0	52.4	241.6	1.6	6.2
			224	25.5	67.5	29.6	2.7	0.2	0.0	88.5	9.5	79.5	355.3	2.3	9.1
			241	34.5	65.8	29.2	4.7	0.3	0.0	81.4	15.8	92.0	378.4	2.5	9.8
Ni_8Pt_1-450	37.2	0.36	209	19.3	69.1	29.8	1.0	0.1	0.0	95.7	3.7	51.2	251.5	1.6	6.8

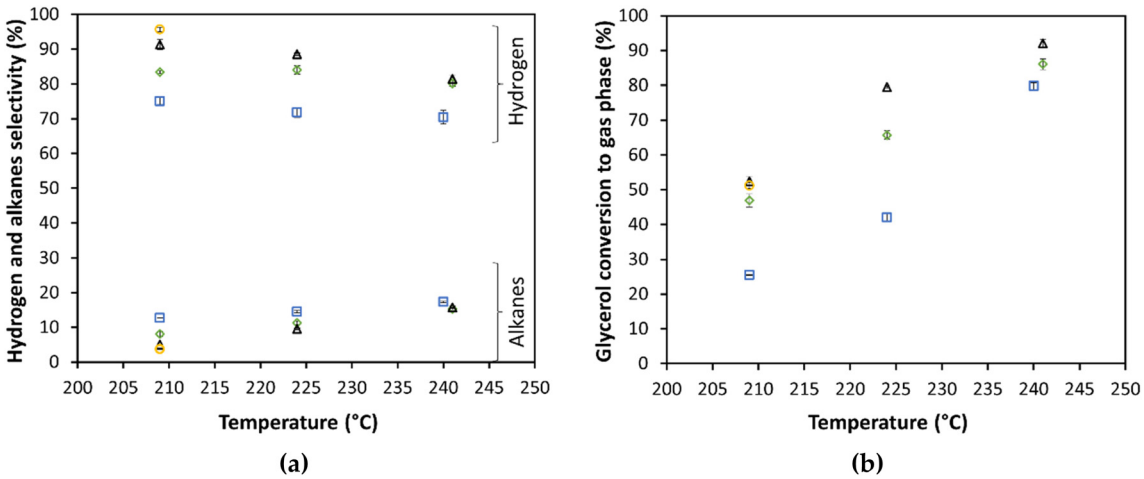

Fig. 6 (a) Hydrogen and Alkanes selectivity, and (b) glycerol conversion to gas phase in the aqueous phase reforming of 10 wt% of glycerol at 0.36 h^{-1} WHSV. □ Pt-260, ◊ Ni_1Pt_1-260, Δ Ni_8Pt_1-260, ○ Ni_8Pt_1-450. Each data point is the mean value of three samples and the standard deviation is indicated by the error bar.

our highest selectivity (95.7%) obtained for Ni_8Pt_1-450 in the APR at 209 °C. In addition, they reported 8 to 10 mol% of methane in the gas product. In this work, we reported (Table 4) that methane mol% is lower than 4.7% for Ni_8Pt_1-260 and as low as 1 mol% for Ni_8Pt_1-450.

Each catalyst shown in Table 4 was studied for APR of 10 wt% glycerol for at least 140 h on stream. The catalyst Pt-260 show no deactivation after 523 h on stream (Fig. S1 in ESI†). Ni_1Pt_1-260 and Ni_8Pt_1-260 show a 10% reduction in glycerol conversion and 5% reduction in H_2 selectivity after 189 h and 140 h on stream, respectively (ESI Fig. S2 and S3†). Ni_8Pt_1-450 shows slow deactivation when the APR was carried out at 209 °C and 19.3 for 401 h on stream. This catalyst had a 15% reduction in glycerol conversion and 4% reduction of H_2 selectivity during the first 40 h of stabilization, as shown in Fig. S4 in ESI.† After the first 40 h, the H_2 selectivity was stable at 91%, as shown in Fig. 7. The gas composition was almost constant at 68% H_2, 30.8% CO_2, 1% methane, and no CO (<10 ppm).

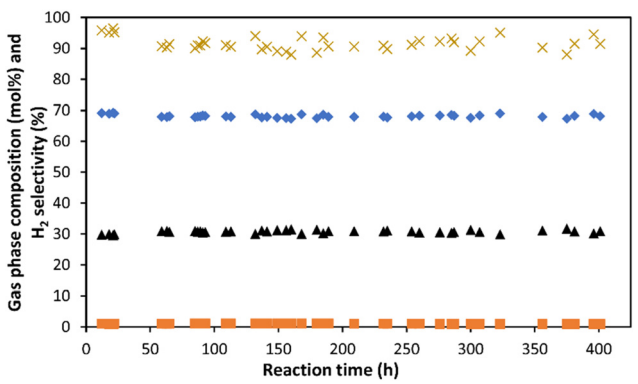

Fig. 7 Gas phase composition (■ Methane, ▲ CO_2, ✦ Hydrogen) and hydrogen selectivity (X) for the Ni_8Pt_1-450 catalyst, in the APR of 10 wt% of glycerol at 0.36 h^{-1} WHSV and 209 °C.

3.3. CO_2 sequestration

The APR of 10 wt% of glycerol over the Ni_8Pt_1-450 catalyst at 209 °C and 0.36 h^{-1} WHSV, was coupled with the CO_2 sequestration over CaO to produce a high-pressure H_2 stream with high purity. Sequestration experiments were conducted: (a) at low CO_2 partial pressure (0.75 bar) in which nitrogen was used as a sweep gas for APR at adsorption temperatures from room temperature to 700 °C with different CaO loadings; and (b) at a higher CO_2 partial pressure (5.3 bar) in which no nitrogen was used as sweep gas.

3.3.1 Isothermal CO_2 sequestration with a low CO_2 partial pressure. The gas stream from the APR unit operated at 209 °C was fed into the CaO bed at 600 °C. CO_2 adsorption was carried out using a packed bed reactor with 50 g of CaO. Minimal CO_2 was taken up at temperatures below 400 °C after 1 h of adsorption. We obtained a stream of H_2 and hydrocarbons with high purity (98.2 mol% of H_2) as shown in Fig. 8. There is complete capture of CO_2 for at least 20 h when the CaO bed is at 600 °C and 700 °C, as shown in Fig. 8a. After this first stage of capture, there is a second stage in which the sequestration rate is lower due to the formation of a layer of $CaCO_3$ over the CaO particles.[79] As shown in Fig. 8b, at 500 °C the CaO saturates after 25 h on stream. For 600 °C and 700 °C the saturation time becomes longer than 100 h. This longer saturation time is related to a higher CO_2 sequestration capacity at these temperatures.

The APR gas product contains less than 10 ppm of CO. From room temperature to 400 °C the CO concentration after the CaO bed was less than 150 ppm. At 500 °C the CO concentration increased to a maximum of 650 ppm at 29 h of adsorption time. As shown in Fig. 8d, the CO concentration increases rapidly during the first few hours of CO_2 adsorption and tends to be constant (0.5 mol% at 500 °C, 8.4 mol% at 600 °C, and 15.5 mol% at 700 °C). CO emissions during the CO_2 capture over CaO are caused due to the presence of H_2. Hydrogen promotes the regeneration of CaO by the decomposition of $CaCO_3$ producing CO and H_2O.[80]

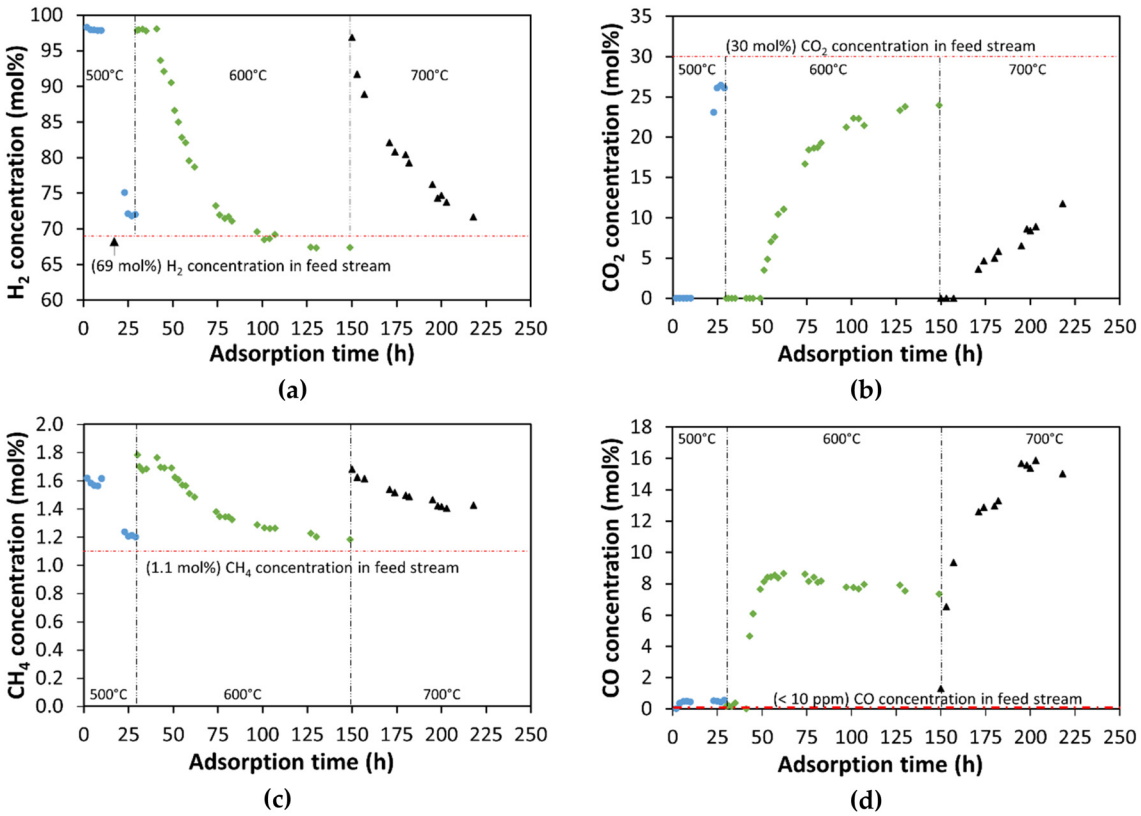

Fig. 8 (a) H_2, (b) CO_2, (c) CH_4, and (d) CO concentrations in the outlet stream of the CO_2 removal bed at 500 °C (•), 600 °C (✦), and 700 °C (▲). The outlet concentrations are reported here on a nitrogen free basis. Packed bed with 50 g of CaO. Inlet gas composition (mol%): 86.8% N_2, 9.1% H_2, 4% CO_2, 0.12% CH_4. CO_2 partial pressure = 0.75 bar. Total molar gas inlet flow = 2.4 mmol min^{-1}.

The CaO adsorption capacity was determined after each isothermal experiment, as shown in Fig. 9. The CaO adsorption capacity was 0.11 mol CO_2/mol CaO at 500 °C, increasing to 0.40 mol CO_2/mol CaO at 600 °C, and finally increasing to 0.65 mol CO_2/mol CaO at 700 °C. These CaO adsorption capacities are lower than the values previously reported by Hlaing *et al.*[66] of 0.87 mol CO_2/mol CaO at 700 °C. However, the required time to obtain this adsorption capacity is around 225 h under these low CO_2 partial pressure (0.75 bar) and total system pressure (19.3 bar). The limitation to achieve a higher CO_2 adsorption capacity at this temperature (700 °C) CO is produced by the reverse water gas shift reaction. Nevertheless, the use of CaO as an adsorbent model indicates that calcium-bearing minerals could be used to capture CO_2, as indicated by Gadikota and Park,[68] by using an *in situ* or *ex situ* carbon mineralization approach.

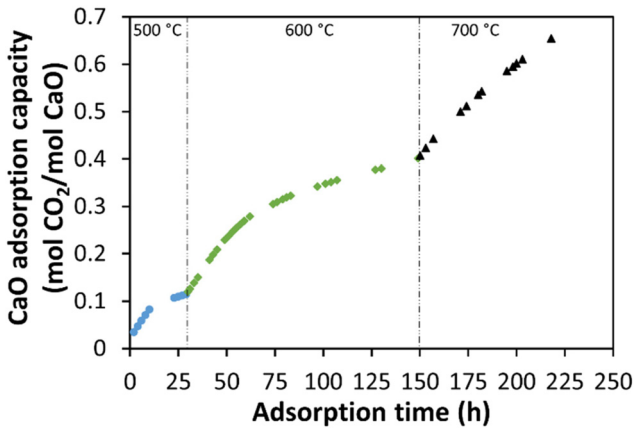

Fig. 9 CaO cumulated adsorption capacity in the capture of CO_2 at 500 °C (•), 600 °C (✦), and 700 °C (▲), during the APR of 10 wt% of glycerol. Packed bed with 50 g of CaO. Inlet gas composition (mol%): 86.8% N_2, 9.1% H_2, 4% CO_2, 0.12% CH_4. CO_2 partial pressure = 0.75 bar. Total molar gas inlet flow = 2.4 mmol min^{-1}.

3.3.2 Isothermal CO_2 sequestration at 600 °C and low CO_2 partial pressure. Additional experiments were carried out to study the CO_2 capture at 600 °C under 0.75 bar of CO_2 partial pressure, with different amounts of CaO with nitrogen as a sweep gas. Complementary information regarding the APR experiment and gas stream fed to the CO_2 adsorber can be found in Fig. S5 of ESI.† Fig. 10a and b show the effluent H_2 and CO_2 concentrations. The CaO bed was saturated with CO_2 after 25 h when 15 g of CaO was packed and in less than an hour for 4 g of CaO. Around 40% of the initial CaO active sites (S_{Tot}) in the bed were carbonated after 40 h of adsorption, as shown in Fig. 10c. The adsorption capacity of CaO is around 0.35 mol CO_2/mol CaO when 15 g of CaO was packed, and

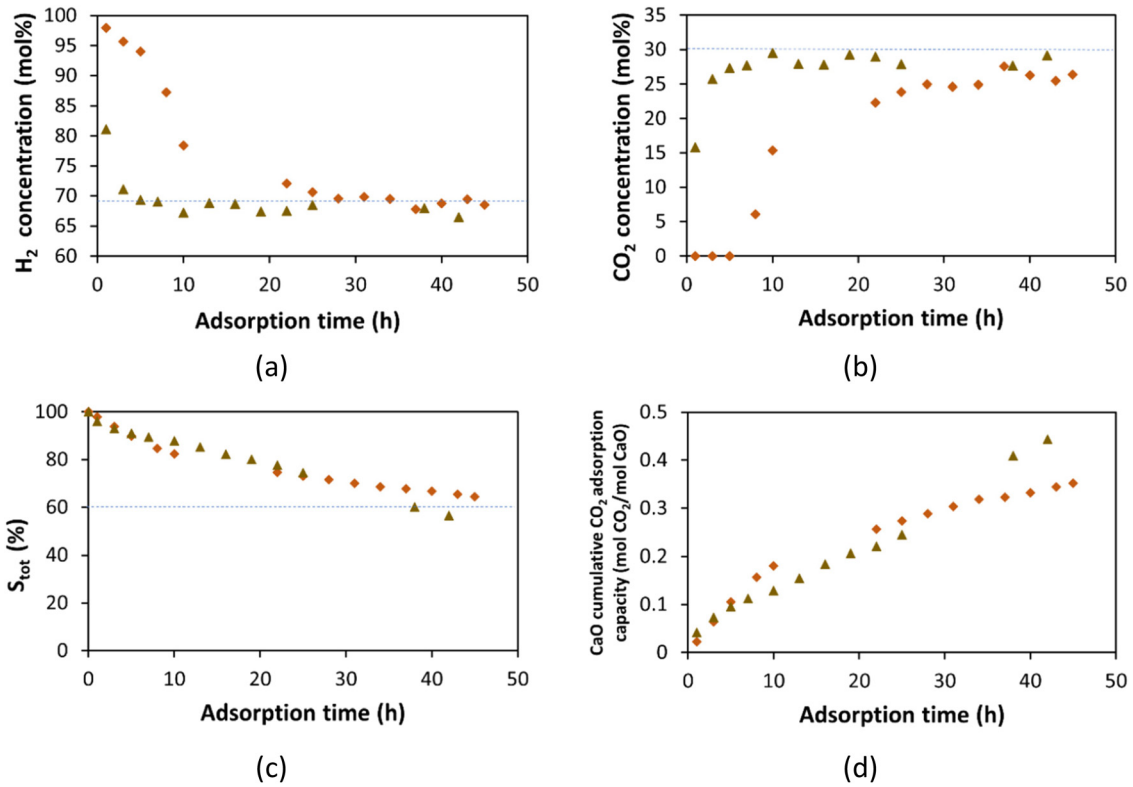

Fig. 10 (a) Hydrogen, and (b) CO_2 concentrations in the outlet stream of the CaO bed at 600 °C on a nitrogen-free basis, (c) changes in the total moles of CaO active sites (S_{tot}) given as a percent of the initial mol of CaO in the adsorber, and (d) the capacity of CaO as mol of CO_2 mol^{-1} of CaO. CaO-packed bed with 4 g (▲) and 15 g (✦) at 0.75 bar of CO_2 partial pressure. Inlet gas composition (mol%): 86.8% N_2, 9.1% H_2, 4% CO_2, 0.12% CH_4. Total molar gas inlet flow = 2.2 mmol min^{-1}.

around 0.4 mol CO_2/mol CaO for 4 g of CaO as shown in Fig. 10d. This behavior agrees with the values obtained when consecutive experiments were carried out at the same temperature. Thus, the sequestration capacity is related to the temperature.

The CO concentration at the outlet of the CO_2 adsorber at 600 °C and an inlet CO_2 partial pressure of 0.75 bar was 3.5 mol% and 4.5 mol% respectively for 4 g and 15 g of CaO packed in the adsorber (see Fig. S6 in ESI† for the whole data collected).

3.3.3 Isothermal CO_2 sequestration at 600 °C with high CO_2 partial pressure. Isothermal CO_2 capture at a high CO_2 partial pressure was carried out with no nitrogen as a sweep gas. Low nitrogen levels with a partial pressure between 0.3 and 1.5 bar were obtained because nitrogen was used to pressurize the system after draining. The partial pressure of CO_2 was kept at an average of 5.3 bar. As shown in Fig. 11 the composition of the gas stream from APR of 10 wt% of glycerol at 209 °C was constant. The catalyst Ni_8Pt_1-450 had good stability during the experiment, with a H_2 selectivity of around 93.1%, and a glycerol conversion to the gas phase of 50%.

Fig. 12a and b show complete CO_2 capture for the first 10 h of operation, producing a high-pressure (19.3 bar) gas stream with 95.5 mol% of H_2 and 4 mol% of methane. There is an apparent CaO saturation after 50 h. The CO_2 mol% in the outlet stream was around 10 mol% lower than the inlet stream at this saturation stage. Once the CaO is saturated, the outlet

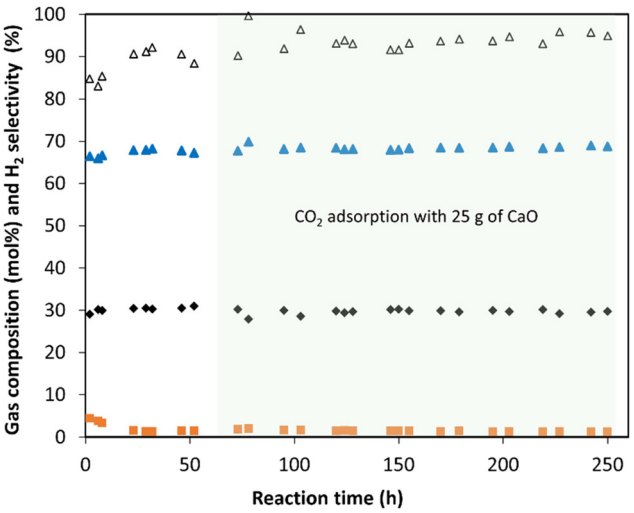

Fig. 11 Inlet gas phase composition (mol%) on a nitrogen-free basis, and hydrogen selectivity (Δ) for the Ni_8Pt_1-450 catalyst, in the APR of 10 wt% of glycerol at 0.36 h^{-1} WHSV, 209 °C and 5.3 bar of CO_2 partial pressure. Gas phase composition: (▲) hydrogen, (✦) CO_2, and (■) methane. Total gas molar inlet flow = 0.81 mmol min^{-1}.

stream should have the same composition as the inlet unless the CO_2 is reacting. Grasa and Abanades[59] reported that CaO derived from natural limestones shows a residual constant

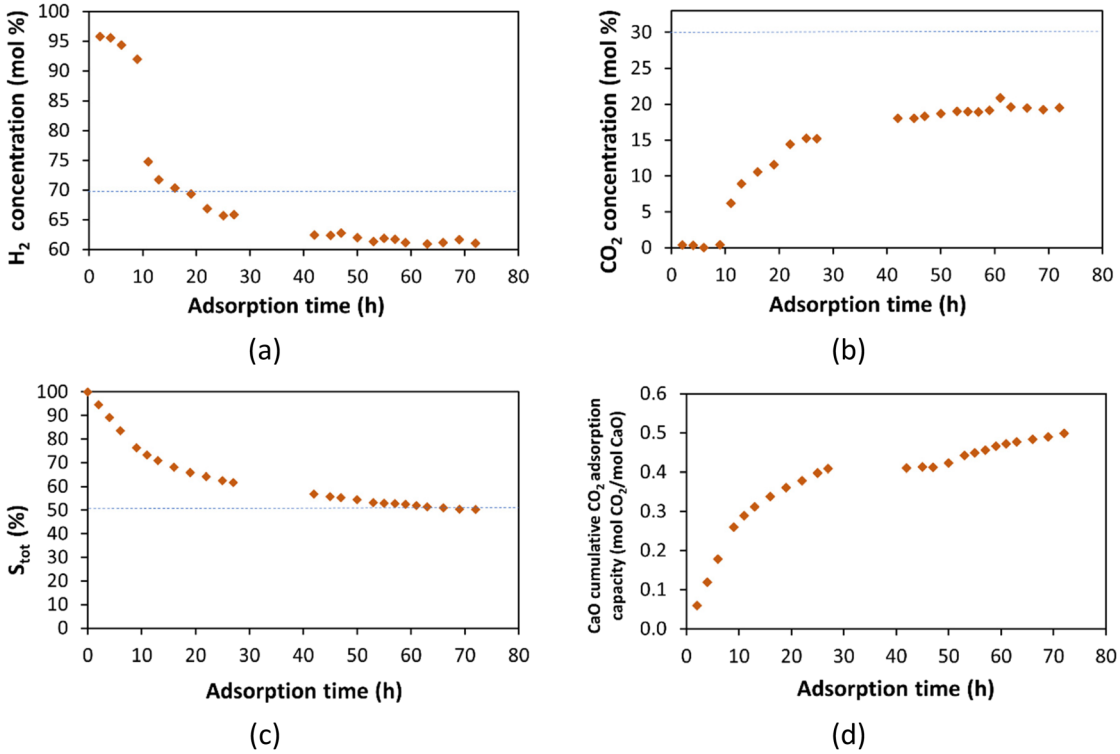

Fig. 12 (a) H_2, and (b) CO_2 concentrations in the outlet stream of the CaO bed at 600 °C, (c) changes in the total moles of CaO active sites (S_{tot}) given as a percent of the initial mol of CaO in the bed, and (d) the adsorption capacity of CaO as mol of CO_2/mol of CaO. CaO-packed bed with 25 g at 5.3 bar of CO_2 partial pressure. Inlet gas composition (mol%): 4.7% N_2, 63.4% H_2, 27.7% CO_2, 1.3% CH_4. Total gas molar inlet flow = 0.81 mmol min^{-1}.

conversion of about 7 to 8% after hundreds of cycles of carbonation/calcination, and seems to be independent of the CaO degradation by calcination temperature. The residual constant conversion is likely related to a catalytic conversion of CO_2 in the CaO. Additionally, Fig. 12c shows that 50% of the initial CaO has reacted at 55 h of adsorption, for a total adsorption capacity of 0.45 mol of CO_2/mol CaO (Fig. 12d). The total CaO active sites (S_{Tot}) and the CaO sequestration capacity were calculated based on the amount of CO_2 adsorbed. To understand this phenomenon, Fig. 13 shows the flow rate of gas phase components for both the inlet and outlet of the CaO bed.

As shown in Fig. 13a, the H_2 flow rate is the same at the inlet and the outlet for the first 9 h, where there is complete CO_2 capture (Fig. 13b). After 9 h of operation, the H_2 flow rate decreases, indicating that H_2 is reacting in the CaO bed. Similarly, the propane (Fig. 13f) flow rate is lower in the outlet stream than in the inlet. The methane and ethane (Fig. 13d and e) flow rates are higher in the outlet stream than in the inlet. These changes in alkane flow rates indicate that propane is being cracked to methane and ethane. These findings indicate that the CaO acts as a catalyst bed at this temperature (600 °C) and pressure (19.3 bar). Table 5 shows the total mol of each component fed to the CaO bed for the 72 h of operation, and the total mol of each component obtained at the outlet stream. H_2, CO_2, and propane were consumed or reacted on the CaO bed, with reductions of 21.8, 60.4, and 54.9% respectively. Meanwhile, methane and ethane increased by around 100%. These changes by the catalytic effect of the CaO in the bed. The CaO catalytic pathways could include (a) CO and water emissions by the $CaCO_3$ decomposition;[81] (b) propane cracking into C1–C2 alkanes; and (c) CO_2 hydrogenation to produce the same C1–C2 alkanes.

At this CO_2 adsorption conditions (600 °C, 19.3 bar of total pressure, and 5.3 bar of CO_2 partial pressure) the CO molar concentration increased from around 0.15 mol% (≈1500 ppm) in the adsorber inlet to around 16 mol% after 10 h of adsorption as can be seen in Fig. S6 of ESI.† The CO production in the CaO bed is affected by the CO_2 partial pressure in the inlet stream in addition to the temperature as discussed previously in section 3.3.1. At 600 °C and 5.3 bar of CO_2 partial pressure, the CO concentration is two times higher than the concentration at the same temperature and 0.75 bar of CO_2 partial pressure, that was 8.4 mol%.

3.3.4 CO_2 sequestration modeling. The CO_2 sequestration constant (k) (or the rate of CO_2 adsorption) was calculated at different adsorption conditions and CaO loadings. Fig. 14 shows that k-values do not depend on the temperature. The k-value is high for the first sequestration stage, in which fast uptake occurs. Values of k for the CO_2 capture at 600 °C decrease from 0.00139 to 0.000189 1 atm per min in the fast stage adsorption. This k-value tends to be constant in slow-stage sequestration.

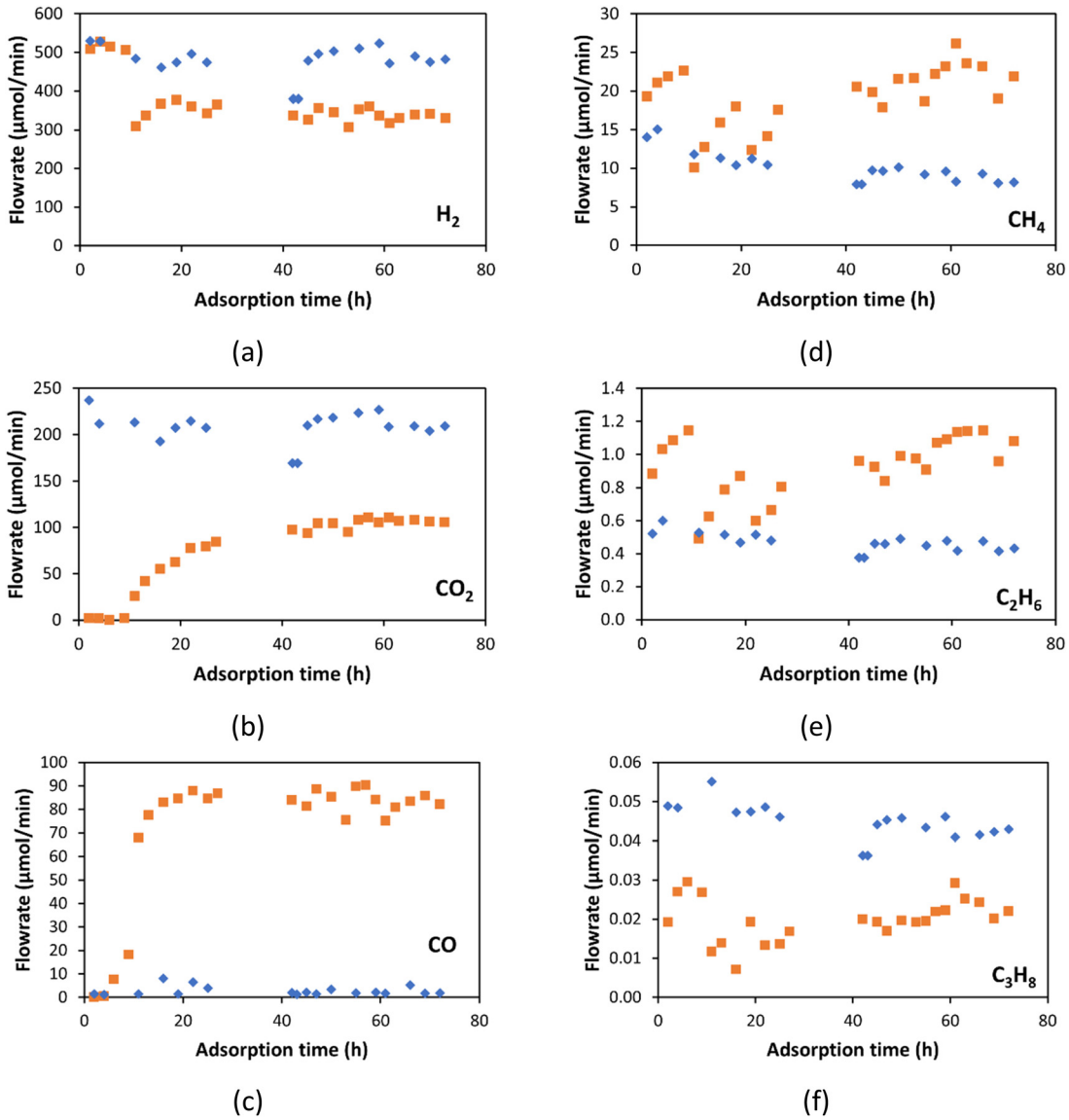

Fig. 13 Inlet (✦) and outlet (■) flowrate of gas components from the CaO bed. (a) H_2, (b) CO_2, (c) CO, (d) CH_4, (e) C_2H_6, and (f) C_3H_8. CaO-packed bed with 25 g at 0.75 bar of CO_2 partial pressure. Inlet gas composition (mol%): 4.7% N_2, 63.4% H_2, 27.7% CO_2, 1.3% CH_4. Total gas molar inlet flow = 0.81 mmol min^{-1}.

Table 5 Total mol of each gas component fed to the CaO bed, the total mol quantified at the outlet, and the change in mol% after 72 h of operation at 600 °C

	Inlet (mol)	Outlet (mol)	Change (%)
H_2	2.01	1.57	−21.8
CO_2	0.87	0.34	−60.4
CO	0.0	0.32	—
Methane	0.04	0.08	100.9
Ethane	2.0×10^{-3}	4.0×10^{-3}	103.9
Propane	1.9×10^{-4}	8.5×10^{-5}	−54.9

Fig. 15 shows the CO_2 sequestration constant (k) calculated when the capture was carried out at 600 °C. The value of k was determined for 4 g, and 15 g of CaO at an inlet CO_2 partial pressure of 0.75 bar; and for a higher CO_2 inlet partial pressure of 5.3 bar with 25 g of CaO. As shown, the k-values have similar values independent of the amount of CaO packed or the CO_2 inlet partial pressure. The k-value was constant at around 0.000165 1 atm per min from 10 to 57 min of adsorption. For the first 10 h of capture, there is a decrease from 0.000897 to 0.000189 1 atm per min, similar to the k-values determined at different temperatures (Fig. 14).

Using a k-value of 0.000165 1 atm per min we calculated the number of CaO active sites at different CO_2 partial pressures (Fig. 16). 0.75 bar and 5.3 bar of inlet CO_2 partial pressures was considered for the calculation at 600 °C.

CaO has been widely proposed for CO_2 capture.[57–65] The CaO sequestration capacity depends on the temperature. Nevertheless, the presence of H_2 causes the reduction of

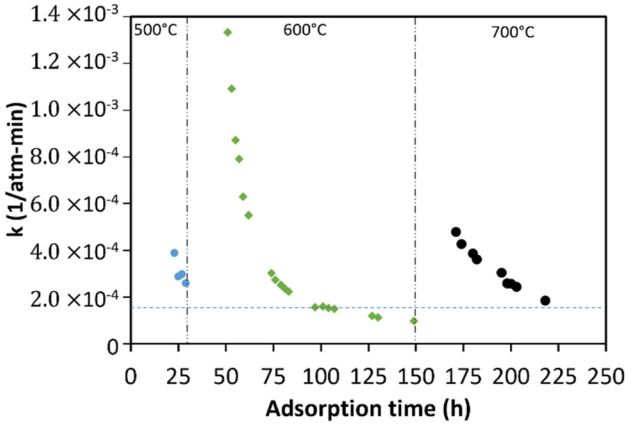

Fig. 14 CO_2 sequestration constant (k) at 500 °C (•), 600 °C (✦), and 700 °C (•) during the APR of 10 wt% of glycerol. Packed bed with 50 g of CaO. Inlet gas composition (mol%): 86.8% N_2, 9.1% H_2, 4% CO_2, 0.12% CH_4. CO_2 partial pressure = 0.75 bar. Total molar gas inlet flow = 2.4 mmol min^{-1}.

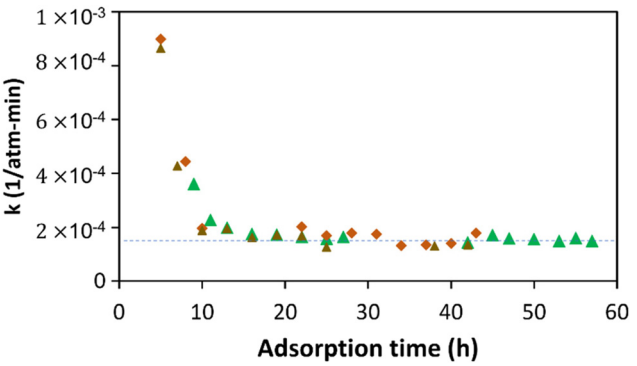

Fig. 15 CO_2 sequestration constant (k) at 600 °C. CaO-packed bed with 4 g (▲) and 15 g (✦) at 0.75 bar of CO_2 partial pressure; inlet gas composition (mol%): 86.8% N_2, 9.1% H_2, 4% CO_2, 0.12% CH_4; and total molar gas inlet flow = 2.23 mmol min^{-1}. ▲ CaO-packed bed with 25 g at 5.3 bar of CO_2 partial pressure; inlet gas composition(mol%): 4.7% N_2, 63.4% H_2, 27.7% CO_2, 1.3% CH_4; and total gas molar inlet flow = 0.81 mmol min^{-1}.

calcium carbonate forming CO and water. As previously reported by Sun *et al.*[80] this effect could be used to produce syngas from flue gases operating the CO_2 adsorber at 600 or 700 °C. But, to keep low CO levels in the H_2 stream while reducing the CO_2 concentrations, it is recommendable to operate the CaO bed at low temperature such as 500 °C or lower, depending on the APR composition and the CO_2 partial pressure. Pressure Swing Adsorption (PSA)[69] was also considered for the LCA and TEA analysis presented below.

3.4. Life cycle assessment (LCA), and techno-economical analysis (TEA)

Fig. 17 presents the results of the LCA analysis in terms of GHG emissions using CaO adsorption (Fig. 17a and c), and PSA (Fig. 17b and d) for two scenarios: Scenario A using Wisconsin grid electricity, and Scenario B using 100% renewable electricity. Wisconsin's electricity generation comes from 44.2% natural gas, 28.8% coal, 17.3% nuclear, and 9.6% renewables.[82] The results are presented considering two impact allocation methods: (i) mass allocation and (ii) carbon content allocation. This figure also shows the GHG contributions of each processing stage in different colors. Based on this analysis, we can observe that all the scenarios result in net negative GHG emissions, except for Scenario A considering allocation by carbon content when CaO is used for CO_2 sequestration at 600 °C. However, CaO adsorption for carbon capture is not currently used industrially. If instead, PSA is used for the hydrogen purification, all the scenarios are carbon negative and with lower GHG emissions compared to the use of CaO at 600 °C. Replacing the electricity grid with renewable energy sources can decrease the GHG emissions of each production stage. Moreover, the allocation method plays a critical role in the resulting GHG emissions. Assumptions taken during the environmental impact analysis, including the allocation method, can significantly alter the analysis results.

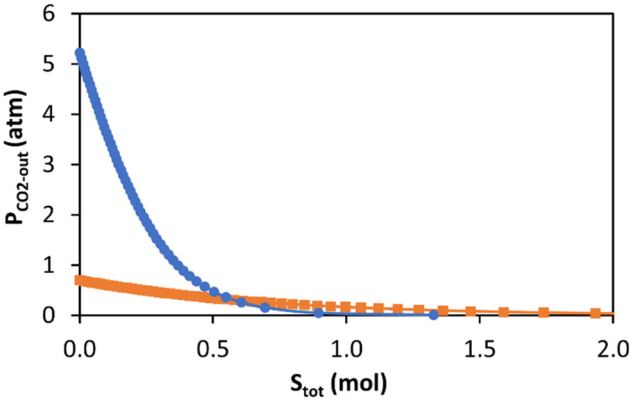

Fig. 16 Relation of the total CaO active sites (S_{tot}) with the CO_2 partial pressure in the CaO bed outlet stream. k = 0.000165 (1 atm per min). • Inlet CO_2 partial pressure of 5.3 atm, 0.208 mmol CO_2 per min, 0.512 mmol H_2 per min, and 0.0599 mmol N_2 per min. ■ Inlet CO_2 partial pressure of 0.75 atm, 0.0882 mmol CO_2 per min, 0.204 mmol H_2 per min, and 2.12 mmol N_2 per min.

Fig. 18 presents a comparison of the APR of glycerol coupled with CCUS considering the mass allocation method compared to other H_2 production technologies. All APR processes have net negative GHG emissions. The high biogenic uptake leads to negative CO_2 emissions for APR processes that use glycerol derived from soybean, thereby contributing to the goal of achieving net-zero carbon emissions. A comparison of all scenarios and both impact allocation methods can be found in Fig. S7 in the ESI.† These results are in accordance with the GHG emissions (−18.5 kg CO_2 eq./kg H_2) reported previously[4] for biomass gasification with CCUS. If Renewable energy is used instead of grid electricity the GHG emissions could be even lower than −50 kg CO_2 eq./kg H_2 under the mass allocation method.

A preliminary techno-economic analysis[83] was conducted to determine the H_2 production costs, including raw material and utility costs. Fig. 19 shows the conceptual design of the industrial-scale APR process coupled with CO_2 sequestration

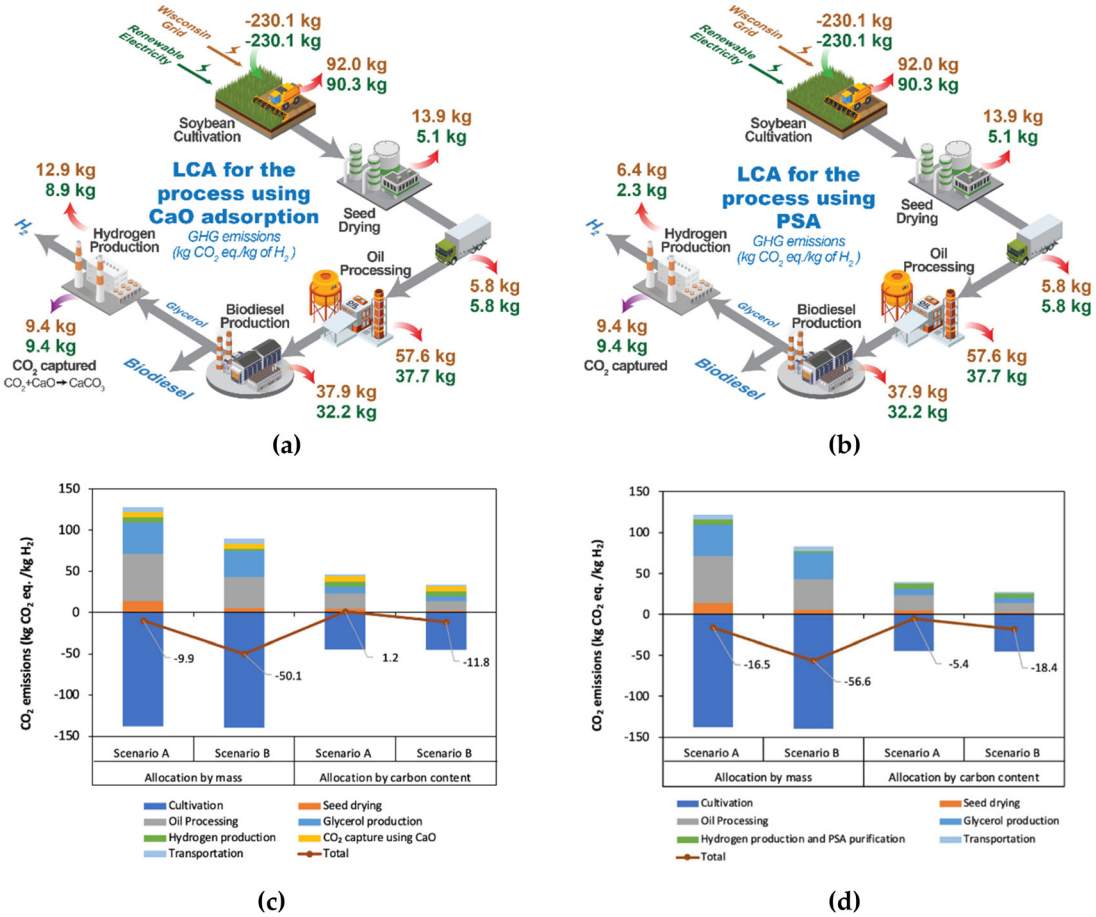

Fig. 17 Hydrogen production pathway and GHG emissions considering mass allocation: (a) CO_2 sequestration over CaO at 600 °C, and (b) using PSA for H_2 purification. The GHG emissions (red arrows), uptake (green arrow), and capture and sequestration (purple arrow) of each production stage are indicated in kg CO_2 eq./kg of H_2 produced under two scenarios, Scenario A: using the Wisconsin grid (brown numbers) and Scenario B: using renewable electricity (green numbers). GHG emissions of all scenarios and the contributions of each production stage to the total GHG emissions considering (c) CO_2 sequestration over CaO at 600 °C, and (d) using PSA for H_2 purification.

using CaO, which was modeled using the Aspen Plus program. The use of CaO for CO_2 sequestration will need an additional step to obtain a high-purity H_2, since the stream obtained still contains small amounts of alkanes and CO (1.8 to 4.4 mol% depending on the CO_2 partial pressure). A small PSA unit could be coupled after the CO_2 sequestration unit using CaO. The process includes four pieces of equipment: a reactor, a flash separator, a fluidized bed reactor, and a compressor. The conceptual design for the industrial-scale APR process coupled with PSA for H_2 purification can be found in Fig. S8 in ESI,† which includes a reactor, a flash separator, a PSA unit, and a compressor. To provide a first estimation of the capital cost, Aspen Capital Cost Estimator was used, which considers various factors such as the size and complexity of each piece of equipment, required materials, and other expenses. These inputs generate calculations of material and energy balances, and capital costs. Based on the calculations, an APR plant producing about 823 000 kg of H_2 per year would require a capital cost of USD 4.3 million and would consume 7112 tons per year of crude glycerol.

Table 6 presents the material and energy costs associated with the operation of the plant based on two scenarios, along with the resulting estimated production cost of the H_2. The transportation cost within Wisconsin is neglected. Results are compared to the target cost of $1 (USD) set by DOE to estimate the desired raw material cost. Based on rough estimates, the price of the 10 wt% glycerol solution needs to be less than 32.4 USD per ton for this technology to produce H_2 at 1 USD per kg. Therefore, glycerol produced from waste oil processing facilities would be the most environmentally and economically favorable.

The current study considers hydrogen production from soybean-based glycerol. However, other common feedstocks are corn stover or lignin-rich stream (LRS) (for example, from cellulosic ethanol production).[88,89] The cost of hydrogen obtained is similar to a study suggesting a price of 1.5 € per kg H_2 produced considering corn stover as feedstock and a hydrothermal liquefaction (HTL)-APR plant.[88] However, when comparing multiple studies, LCA and TEA values can vary extremely depending on the system considerations, scope, and

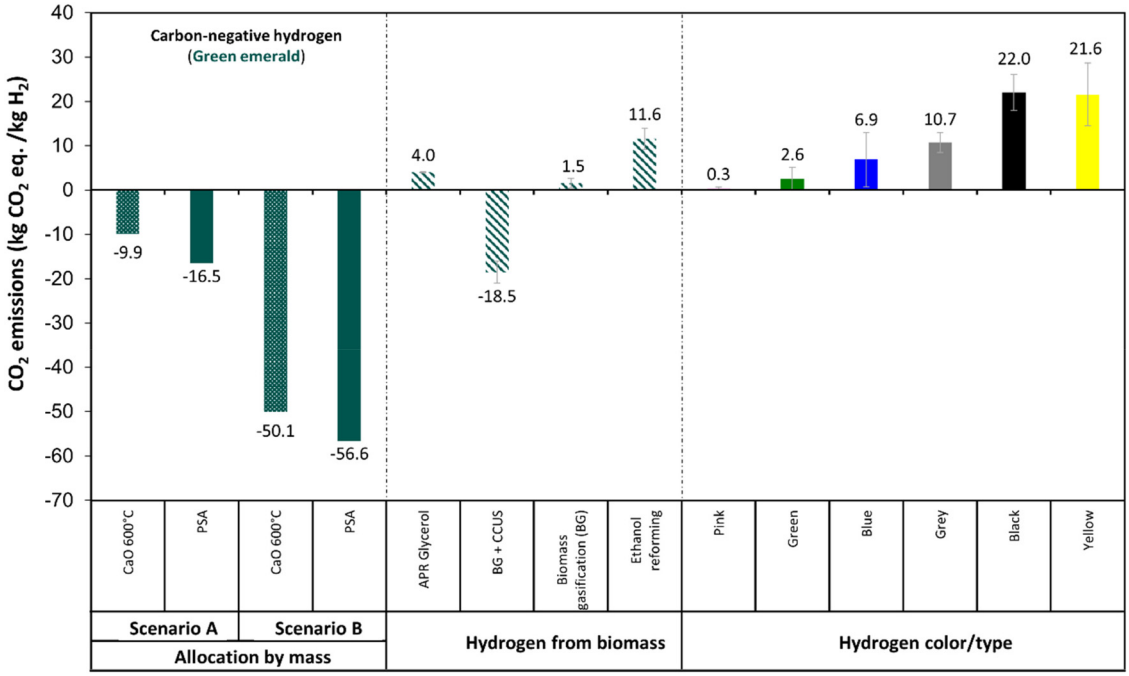

Fig. 18 Comparison of GHG emissions of H_2 production technology presented in this work with the technologies presented in Table 1. Scenario A: using Wisconsin grid electricity. Scenario B: using 100% renewable electricity.

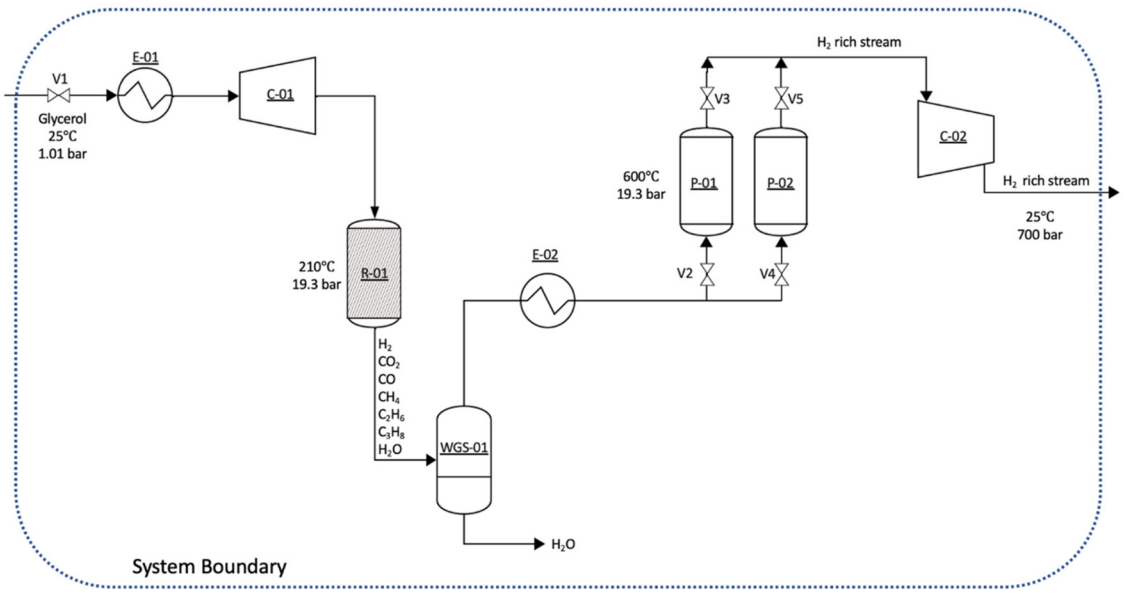

Fig. 19 Process scheme of APR of glycerol to produce H_2 analyzed in TEA considering CaO adsorption.

boundaries.[14,88,90,91] Most studies assessing H_2 production using APR technology don't perform LCA and TEA together. However, a recent study[92] demonstrated a 60% reduction (from 20.9 to 8.2 g CO_2 eq. per MJ) in GHG emissions (mass allocation method) on sustainable aviation fuel production, and a 17% reduction (2.20 to 1.84 $ per kg) in the minimum fuel selling price of SAF when hydrogen was produced *in situ* through APR of glycerol. This demonstrates that hydrogen produced through APR technology can help to reduce GHG emissions and costs when coupled with other processes.

The cost of H_2 production can be reduced by considering carbon credits. It should be noted that the market price of CO_2 fluctuates over time. As shown in Fig. 20 for the H_2 cost estimated for APR CO_2 separation using PSA, if CO_2 is sold back at the California carbon credit market price, the production cost of H_2 is 2.38 USD per kg H_2 with grid electricity and 2.17 USD

Table 6 Estimated production costs and its target include raw material, utility, and transportation costs. Scenario A: using Wisconsin grid electricity. Scenario B: using renewable electricity

	Using PSA		Using CaO		
	Scenario A	Scenario B	Scenario A	Scenario B	The goal of 1 USD per kg H_2
Price of glycerol solution (USD per ton)	198 [84]	198 [84]	198 [84]	198 [84]	32.4
Raw material cost: glycerol (USD per kg H_2)	1.71	1.71	1.71	1.71	0.28
Heat cost (USD per kg H_2)	0.13 [85]	0.13 [85]	0.22 [85]	0.22 [85]	0.22 [85]
Electricity cost (USD per kg H_2)	0.50 [86]	0.72 [87]	0.50 [86]	0.72 [87]	0.50 [86]
H_2 cost (USD per kg H_2)	2.3	2.6	2.4	2.7	1

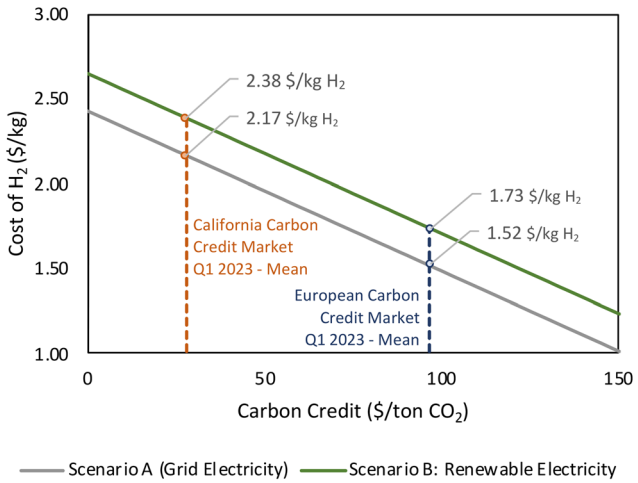

Fig. 20 The production cost of H_2 if different carbon credits are applied. Costs estimated for H_2 produced in the APR of glycerol at 209 °C and 19.3 bar, using PSA for CO_2 separation and H_2 purification.

per kg H_2 with renewable electricity. The production cost is even lower if it is sold at the European market price; the production cost of H_2 is 1.73 USD per kg H_2 with grid electricity and 1.52 USD per kg H_2 with renewable electricity.

This study was carried out considering the glycerol produced as a byproduct in the state of Wisconsin (USA), which was around 7112 tons and represents only around 1.5% of the total production in the United States in 2023. According to the U.S. Energy Information Administration[93] the total biodiesel production in the United States in 2023 was around 6500 million litres, which generates 566 000 tons of glycerol. This amount of glycerol can lead to the production of around 65 000 ton of green-emerald H_2 in the U.S., representing 0.5% of the total Hydrogen demand in 2020 in the U.S. according to the data of McKinsey & Company.[94]

The estimated global demand for biodiesel in 2027 will be 52 billion litres[95] which corresponds to 4.6 million tons of glycerol. This amount of glycerol can produce 530 000 tons of H_2, which represents 0.6% of the global hydrogen demand. In addition to glycerol, this technology could be applied to other more abundant biomass feedstocks such as ethanol, xylitol, sorbitol, xylose, cellulose, or the whole biomass. This availability is especially important to achieve the goal of net-zero carbon emissions, and to diversify the renewable hydrogen sources.

4. Conclusions

Carbon-negative H_2, or green-emerald H_2, can be produced by coupling APR technology with CO_2 sequestration. APR of glycerol at 209 °C using a Ni_8Pt_1-450 catalyst with a system pressure 0.5 bar above the bubble point of water had a H_2 selectivity of 95.7%. The carbon-negative H_2 stream obtained after CO_2 sequestration had 98.2 mol% H_2 purity and 1.8 mol% methane. For higher CO_2 partial pressure and no nitrogen as sweep gas, the carbon-negative H_2 purity was 95.6 mol%, with 3.8 mol% methane and 0.2% ethane. CO concentrations of 400 and 800 ppm were detected respectively. Calcium oxide had an adsorption capacity of 0.35–0.4 mol CO_2/mol CaO at 600 °C for low CO_2 partial pressure. The CaO can catalyze the formation of CO by reverse water gas shift reaction at higher adsorption capacity and CO_2 partial pressures.

From the LCA analysis, the total GHG emissions depend on the key assumptions and allocation method applied. The analysis showed that APR coupled with CCUS could produce H_2 with net negative GHG emissions, especially considering the use of renewable energy. Future research will investigate different shares of renewable energy and their effect on GHG emissions and economic impacts. The GHG emissions can be as low as −50.1 kg CO_2/kg H_2 using CaO at 600 °C, and as low as −56.6 kg CO_2/kg H_2 using PSA when renewable electricity is used according to the allocation by mass in both cases. Our carbon-negative H_2 has a lower carbon footprint than other reported methods to produce H_2.[2–7,9,14] Therefore, the APR of biomass-derived feedstocks coupled with CCUS can help to achieve the US DOE target of net-zero carbon emissions. TEA analysis indicates that the crude glycerol price needs to be lower than 32.4 USD per ton to produce H_2 at 1 USD per kg H_2.

Author contributions

Leoncio Santiago-Martínez contributed conceptualization, methodology, data curation, formal analysis, investigation, validation, visualization, writing – original draft preparation, writing – review and editing; Mengting Li contributed methodology, investigation, data curation, visualization, and writing – original draft preparation; Paola Munoz-Briones contributed investigation, data curation, and writing – review and editing;

Javiera Vergara-Zambrano contributed investigation, data curation, visualization, and writing – review and editing; Styliani Avraamidou contributed conceptualization, resources, data curation, formal analysis, supervision, validation, investigation, methodology, funding acquisition, and writing – review and editing; James A. Dumesic contributed conceptualization, resources, formal analysis, supervision, funding acquisition, validation, methodology, project administration, and writing – review and editing; and George W. Huber contributed conceptualization, resources, formal analysis, supervision, funding acquisition, validation, methodology, project administration, writing – original draft preparation, and writing – review and editing.

Conflicts of interest

The authors declare no conflict of interest.

Acknowledgements

The authors gratefully thank Professor Bu Wang for his valuable comments on CO_2 sequestration. This material is based upon work supported by the DOE Great Lakes Bioenergy Research Center (Award Number DE-SC0018409) and by the DOE Center for Advanced Bioenergy and Bioproducts Innovation (Award Number DE-SC0018420), U.S. Department of Energy, Office of Science, Office of Biological and Environmental Research.

References

1 International Energy Agency (IEA), The Future of Hydrogen. Seizing today's opportunities. Report prepared by the IEA for the G20, Japan.
2 M. M. Mohideen, B. Subramanian, J. Sun, J. Ge, H. Guo, A. V. Radhamani, S. Ramakrishna and Y. Liu, *Renewable Sustainable Energy Rev.*, 2023, **174**, 113153.
3 A. Mehmeti, A. Angelis-Dimakis, G. Arampatzis, S. J. McPhail and S. Ulgiati, *Environments*, 2018, **5**, 1–19.
4 International Energy Agency (IEA), *Towards Hydrogen Definitions Based on their Emissions Intensity*, France, 2023.
5 A. Ajanovic, M. Sayer and R. Haas, *Int. J. Hydrogen Energy*, 2022, **47**, 24136–24154.
6 J. M. M. Arcos and D. M. F. Santos, *Gases*, 2023, **3**, 25–46.
7 P. Burmistrz, T. Chmielniak, L. Czepirski and M. Gazda-Grzywacz, *J. Cleaner Prod.*, 2016, **139**, 858–865.
8 GEI (Global Energy Infrastructure), Hydrogen – data telling a story, **https://globalenergyinfrastructure.com/articles/2021/03-march/hydrogen-data-telling-a-story/**, (accessed 10 March 2023).
9 M. Yu, K. Wang and H. Vredenburg, *Int. J. Hydrogen Energy*, 2021, **46**, 21261–21273.
10 A. Willige, *Spectra*, Miitsubishi Heavy Ind. Gr., 2022.
11 E. Hand, *Science*, 2023, **379**, 630–636.
12 CEMVITA, Gold Hydrogen, **https://www.cemvita.com/gold-hydrogen**, (accessed 3 August 2023).
13 F. Osselin, C. Soulaine, C. Fauguerolles, E. C. Gaucher, B. Scaillet and M. Pichavant, *Nat. Geosci.*, 2022, **15**, 765–769.
14 Y. F. Khalil, *Clean Energy*, 2021, **5**, 387–402.
15 S. McQueen, J. Stanford, S. Satyapal, E. Miller, N. Stetson, D. Papageorgopoulos, N. Rustagi, V. Arjona, J. Adams, K. Randolph, D. Peterson, L. Hill, M. Koleva, T. Reinhardt, E. Frye, R. Schrecengost, A. Kokkinos, J. Litynski, R. Conrad, G. Soloveichik, D. Tew, S. Litzelman, J. Vetrano, R. Onuschak, A. Hahn, E. Hsieh and R. Costa, *Department of Energy Hydrogen Program Plan*, 2020, DOI: **10.2172/1721803**.
16 C. D. Scown, *Trends Biotechnol.*, 2022, **40**, 1415–1424.
17 J. W. Shabaker, R. R. Davda, G. W. Huber, R. D. Cortright and J. A. Dumesic, *J. Catal.*, 2003, **215**, 344–352.
18 G. W. Huber, J. W. Shabaker, S. T. Evans and J. A. Dumesic, *Appl. Catal., B*, 2006, **62**, 226–235.
19 R. R. Davda and J. A. Dumesic, *Angew. Chem., Int. Ed.*, 2003, **42**, 4068–4071.
20 R. D. Cortright, R. R. Davda and J. A. Dumesic, *Nature*, 2002, **418**, 964–967.
21 R. R. Davda, J. W. Shabaker, G. W. Huber, R. D. Cortright and J. A. Dumesic, *Appl. Catal., B*, 2003, **43**, 13–26.
22 J. W. Shabaker, G. W. Huber, R. R. Davda, R. D. Cortright and J. A. Dumesic, *Catal. Lett.*, 2003, **88**, 226–235.
23 M. S. Masnadi, J. R. Grace, X. T. Bi, N. Ellis, C. J. Lim and J. W. Butler, *Energy*, 2015, **83**, 326–336.
24 L. Han, Q. Wang, Z. Luo, N. Rong and G. Deng, *Appl. Energy*, 2013, **109**, 36–43.
25 B. Li, H. Yang, L. Wei, J. Shao, X. Wang and H. Chen, *Int. J. Hydrogen Energy*, 2017, **42**, 5840–5848.
26 C. Xu, S. Chen, A. Soomro, Z. Sun and W. Xiang, *J. Energy Inst.*, 2018, **91**, 805–816.
27 M. H. Doranehgard, H. Samadyar, M. Mesbah, P. Haratipour and S. Samiezade, *Fuel*, 2017, **202**, 29–35.
28 M. B. Valenzuela, C. W. Jones and P. K. Agrawal, *Energy and Fuels*, 2006, **20**, 1744–1752.
29 B. Meryemoglu, A. Hesenov, S. Irmak, O. M. Atanur and O. Erbatur, *Int. J. Hydrogen Energy*, 2010, **35**, 12580–12587.
30 J. Zhang, W. Yan, Z. An, H. Song and J. He, *ACS Sustainable Chem. Eng.*, 2018, **6**, 7313–7324.
31 G. Wen, Y. Xu, Q. Liu, C. Wang, H. Liu and Z. Tian, *Catal. Lett.*, 2011, **141**, 1851–1858.
32 G. Wen, Y. Xu, Z. Xu and Z. Tian, *Catal. Commun.*, 2010, **11**, 522–526.
33 T. Soták, M. Hronec, I. Vávra and E. Dobročka, *Int. J. Hydrogen Energy*, 2016, **41**, 21936–21944.
34 G. Pipitone, G. Zoppi, A. Frattini, S. Bocchini, R. Pirone and S. Bensaid, *Catal. Today*, 2020, **345**, 267–279.
35 C. H. Lee, M. K. Kim, S. Kim, S. W. Choi, H. W. Kim, J. Jae, H. Sohn, S. H. Choi, S. P. Yoon, K. B. Lee and H. C. Ham, *Int. J. Energy Res.*, 2022, **46**, 14478–14490.

36 Y. Kim, M. Kim, H. Jeong, Y. Kim, S. H. Choi, H. C. Ham, S. W. Lee, J. Y. Kim, K. H. Song, C. W. Yoon, Y. S. Jo and H. Sohn, *Int. J. Hydrogen Energy*, 2020, **45**, 13848–13861.
37 M. El Doukkali, A. Iriondo, J. F. Cambra, L. Jalowiecki-Duhamel, A. S. Mamede, F. Dumeignil and P. L. Arias, *J. Mol. Catal. A: Chem.*, 2013, **368–369**, 125–136.
38 M. El Doukkali, A. Iriondo, N. Miletic, J. F. Cambra and P. L. Arias, *Int. J. Hydrogen Energy*, 2017, **42**, 23617–23630.
39 L. Zhang, A. M. Karim, M. H. Engelhard, Z. Wei, D. L. King and Y. Wang, *J. Catal.*, 2012, **287**, 37–43.
40 A. Wawrzetz, B. Peng, A. Hrabar, A. Jentys, A. A. Lemonidou and J. A. Lercher, *J. Catal.*, 2010, **269**, 411–420.
41 Y. Guo, X. Liu, M. U. Azmat, W. Xu, J. Ren, Y. Wang and G. Lu, *Int. J. Hydrogen Energy*, 2012, **37**, 227–234.
42 A. Ciftci, B. Peng, A. Jentys, J. A. Lercher and E. J. M. Hensen, *Appl. Catal., A*, 2012, **431–432**, 113–119.
43 M. M. Rahman, T. L. Church, A. I. Minett and A. T. Harris, *ChemSusChem*, 2013, **6**, 1006–1013.
44 A. J. Reynoso, U. Iriarte-velasco, M. A. Guti and J. L. Ayastuy, *Catal. Today*, 2021, **367**, 278–289.
45 D. L. King, L. Zhang, G. Xia, A. M. Karim, D. J. Heldebrant, X. Wang, T. Peterson and Y. Wang, *Appl. Catal., B*, 2010, **99**, 206–213.
46 N. Luo, X. Fu, F. Cao, T. Xiao and P. P. Edwards, *Fuel*, 2008, **87**, 3483–3489.
47 A. Ciftci, D. A. J. M. Ligthart and E. J. M. Hensen, *Green Chem.*, 2014, **16**, 853–863.
48 T.-W. Kim, H.-D. Kim, K.-E. Jeong, H.-J. Chae, S.-Y. Jeong, C.-H. Lee and C.-U. Kim, *Green Chem.*, 2011, **13**, 1718–1728.
49 L.-J. Zhu, P.-J. Guo, X.-W. Chu, S.-R. Yan, M.-H. Qiao, K.-N. Fan, X.-X. Zhang and B.-N. Zong, *Green Chem.*, 2008, **10**, 1323–1330.
50 F. Bastan, M. Kazemeini, A. Larimi and H. Maleki, *Int. J. Hydrogen Energy*, 2018, **43**, 614–621.
51 A. S. Larimi, M. Kazemeini and F. Khorasheh, *Appl. Catal., A*, 2016, **523**, 230–240.
52 A. S. Larimi, M. Kazemeini and F. Khorasheh, *Int. J. Hydrogen Energy*, 2016, **41**, 17390–17398.
53 G. Wen, Y. Xu, H. Ma, Z. Xu and Z. Tian, *Int. J. Hydrogen Energy*, 2008, **33**, 6657–6666.
54 J. Remón, J. Ruiz, M. Oliva, L. García and J. Arauzo, *Chem. Eng. J.*, 2016, **299**, 431–448.
55 L. A. Dosso, C. R. Vera and J. M. Grau, *Int. J. Hydrogen Energy*, 2017, **42**, 18853–18864.
56 C. He, J. Zheng, K. Wang, H. Lin, J. Y. Wang and Y. Yang, *Appl. Catal., B*, 2015, **162**, 401–411.
57 Y. A. Criado, B. Arias and J. C. Abanades, *Ind. Eng. Chem. Res.*, 2018, **57**, 12595–12599.
58 F. D. M. Daud, K. Vignesh, S. Sreekantan and A. R. Mohamed, *New J. Chem.*, 2016, **40**, 231–237.
59 G. S. Grasa and J. C. Abanades, *Ind. Eng. Chem. Res.*, 2006, **45**, 8846–8851.
60 M. Rydén and P. Ramos, *Fuel Process. Technol.*, 2012, **96**, 27–36.
61 Z. Skoufa, A. Antzara, E. Heracleous and A. A. Lemonidou, *Energy Procedia*, 2016, **86**, 171–180.
62 H. Sun, J. Wang, X. Liu, B. Shen, C. M. A. Parlett, G. O. Adwek, E. John Anthony, P. T. Williams and C. Wu, *J. Mater. Chem. A*, 2019, **7**, 9977–9987.
63 S. Turrado, B. Arias, J. R. Fernández and J. C. Abanades, *Ind. Eng. Chem. Res.*, 2018, **57**, 13372–13380.
64 M. Liu, A. Hohenshil and G. Gadikota, *Energy Fuels*, 2021, **35**, 8051–8068.
65 F. N. Ridha, V. Manovic, A. Macchi and E. J. Anthony, *Appl. Energy*, 2015, **140**, 297–303.
66 N. N. Hlaing, S. Sreekantan, H. Hinode, W. Kurniawan, A. A. Thant, R. Othman, A. R. Mohamed and C. Salime, *AIP Conf. Proc.*, 2016, **1733**, 020023.
67 T. Yin, S. Yin, A. Srivastava and G. Gadikota, *Resour., Conserv. Recycl.*, 2022, **180**, 106209.
68 G. Gadikota and A. A. Park, in *Carbon Dioxide Utilisation: Closing the Carbon Cycle: First Edition*, ed. P. Styring, A. A. Quadrelli and K. Armstrong, Elsevier, 2015, pp. 115–137.
69 C. A. Grande, in *Hydrogen Science and Engineering: Materials, Processes, Systems and Technology*, ed. D. Stolten and B. Emonts, Wiley-VCH, Germany, 2016, pp. 489–508.
70 I. Leinonen, *Int. J. Life Cycle Assess.*, 2022, **27**, 1038–1043.
71 J. H. Schmidt, *J. Cleaner Prod.*, 2015, **87**, 130–138.
72 Omni Tech International, *Life Cycle Impact of Soybean Production and Soy Industrial Products*, 2010.
73 N. Jungbluth, M. Faist Emmenegger, F. Dinkel, C. Stettler, G. Doka, M. Chudacoff, A. Dauriat, E. Gnansounou, M. Spielmann, J. Sutter, N. Kljun, M. Keller and K. Schleiss, *Life cycle inventories of bioenergy*, 2007.
74 J. Dufour and D. Iribarren, *Renewable Energy*, 2012, **38**, 155–162.
75 T. D. Alcock, D. E. Salt, P. Wilson and S. J. Ramsden, *Sci. Total Environ.*, 2022, **829**, 154539.
76 M. M. Rahman, T. L. Church, M. F. Variava, A. T. Harris and A. I. Minett, *RSC Adv.*, 2014, **4**, 18951–18960.
77 A. Tanksale, C. H. Zhou, J. N. Beltramini and G. Q. Lu, *J. Inclusion Phenom. Macrocyclic Chem.*, 2009, **65**, 83–88.
78 A. Morales-Marín, J. L. Ayastuy, U. Iriarte-Velasco and M. A. Gutiérrez-Ortiz, *Appl. Catal., B*, 2019, **244**, 931–945.
79 D. Alvarez and J. C. Abanades, *Ind. Eng. Chem. Res.*, 2005, **44**, 5608–5615.
80 S. Sun, Z. Lv, Y. Qiao, C. Qin, S. Xu and C. Wu, *Carbon Capture Sci. Technol.*, 2021, **1**, 1–4.
81 S. Sun, Z. Lv, Y. Qiao, C. Qin, S. Xu and C. Wu, *Carbon Capture Sci. Technol.*, 2021, **1**, 100001.
82 U.S. Energy, Information Administration (EIA), Wisconsin State Energy Profile, **https://www.eia.gov/state/print.php?sid=WI**, (accessed 12 March 2024).
83 C. D. Scown, N. R. Baral, M. Yang, N. Vora and T. Huntington, *Curr. Opin. Biotechnol.*, 2021, **67**, 58–64.
84 Selina Wamucii, US Glycerol Prices, **https://www.selinawamucii.com/insights/prices/united-states-of-america/glycerol/#:~:text=In2022%2C** the approximate price, in New York and Washington, (accessed 13 December 2022).
85 Natural Gas2022 data – 1990-2021 historical – 2023 forecast – price – quote – chart, **https://tradingeconomics.**

com/commodity/natural-gas, (accessed 13 December 2022).
86 Electricity Local, Wisconsin Electricity Rates and Consumption, https://www.electricitylocal.com/states/wisconsin/, (accessed 13 December 2022).
87 IRENA, *Int. Renewable Energy Agency*, 2012, **1**, 44.
88 E. Tito, G. Zoppi, G. Pipitone, E. Miliotti, A. Di Fraia, A. M. Rizzo, R. Pirone, D. Chiaramonti and S. Bensaid, *J. Environ. Chem. Eng.*, 2023, **11**, 109076.
89 G. Zoppi, E. Tito, I. Bianco, G. Pipitone, R. Pirone and S. Bensaid, *Renewable Energy*, 2023, **206**, 375–385.
90 D. A. Sladkovskiy, L. I. Godina, K. V. Semikin, E. V. Sladkovskaya, D. A. Smirnova and D. Y. Murzin, *Chem. Eng. Res. Des.*, 2018, **134**, 104–116.
91 M. Khodabandehloo, A. Larimi and F. Khorasheh, *Energy Convers. Manage.*, 2020, **225**, 113483.
92 G. Pipitone, G. Zoppi, R. Pirone and S. Bensaid, *J. Cleaner Prod.*, 2023, **418**, 138141.
93 U.S. Energy, Information Administration (EIA), Monthly Energy Review, https://www.eia.gov/totalenergy/data/monthly/pdf/mer.pdf, (accessed 9 April 2024).
94 G. Chiara, H. Bernd, N. Jesse and W. Maurits, Global Energy Perspective 2023: Hydrogen Outlook, https://www.mckinsey.com/industries/oil-and-gas/our-insights/global-energy-perspective-2023-hydrogen-outlook#/, (accessed 9 April 2024).
95 International Energy Agency (IEA), *Renewables 2022, Analysis and forecast to 2027*, France, 2022.